

¹
² Susceptible host dynamics explain pathogen resilience to
³ perturbations

⁴
⁵ Sang Woo Park, . . . , Bryan T. Grenfell, Sarah Cobey

⁶ Abstract

⁷ Major priority for epidemiological research in the time of anthropogenic change is un-
⁸ derstanding how infectious disease dynamics respond to perturbations. Interventions
⁹ to slow the spread of SARS-CoV-2 significantly disrupted the transmission of other
¹⁰ human pathogens. As interventions lifted, whether and when respiratory pathogens
¹¹ would eventually return to their pre-pandemic dynamics remains to be answered. We
¹² develop a framework for estimating pathogen resilience based on how fast epidemic
¹³ patterns return to their pre-pandemic, endemic dynamics. Our analysis suggests
¹⁴ that some pathogens may have settled to endemic cycles that are different from their
¹⁵ pre-pandemic patterns. Finally, we show that the replenishment rate of the suscep-
¹⁶ tible pool is a key determinant of pathogen resilience. Our framework offers a novel
¹⁷ perspective to characterizing the dynamics of endemic pathogens and their responses
¹⁸ to SARS-CoV-2 interventions. **[SWP: Need to emphasize broader implications.]**

19 Non-pharmaceutical interventions (NPIs) to slow the spread of SARS-CoV-2 disrupted
 20 the transmission of other human respiratory pathogens, adding uncertainties to their future epidemic dynamics and the overall public health burden [1].
 21 As NPIs lifted, large heterogeneities in outbreak dynamics were observed across
 22 different pathogens in different countries, with some pathogens exhibiting earlier
 23 resurgences than others [2, 3, 4]. Heterogeneities in the overall reduction in trans-
 24 mission and the timing of re-emergence likely reflect differences in NPI patterns,
 25 pathogen characteristics, immigration/importation from other countries, and pre-
 26 NPI pathogen dynamics [5]. Therefore, comparing the differential impact of the
 27 pandemic NPIs across pathogens can provide unique opportunities to learn about
 28 underlying pathogen characteristics, such as their transmissibility or duration of im-
 29 munity, from heterogeneities in re-emergence patterns [6].

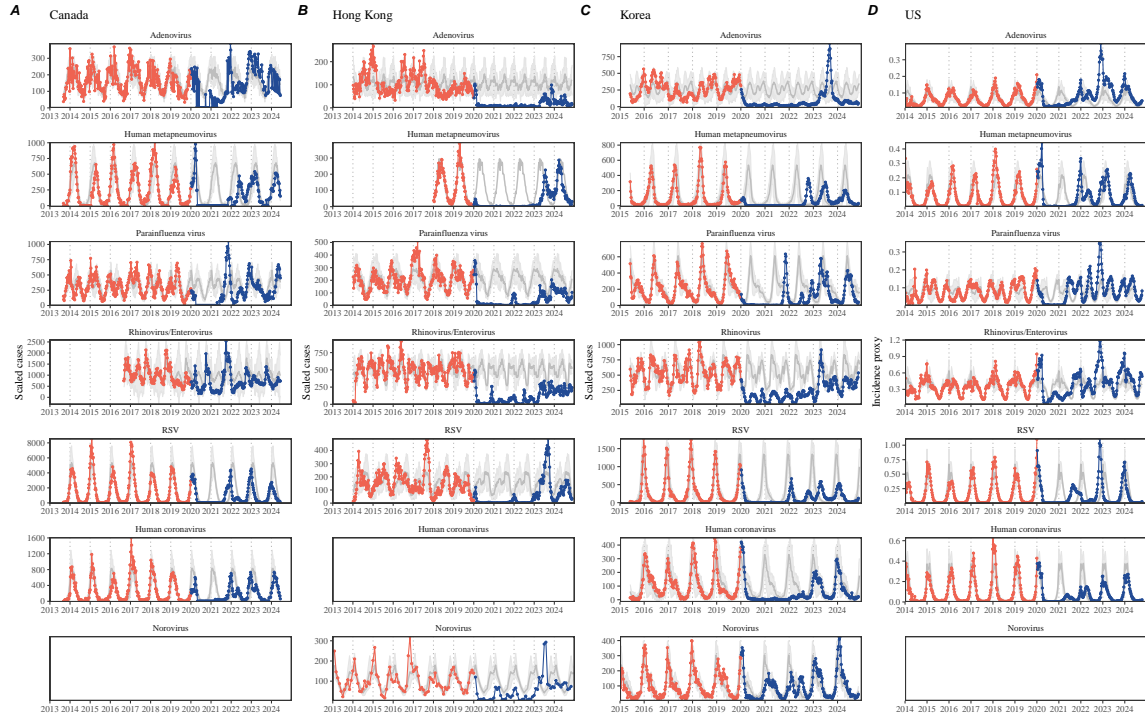


Figure 1: Observed heterogeneity in responses to pandemic NPIs across respiratory pathogens and norovirus in (A) Canada, (B) Hong Kong, (C) Korea, and (D) US. Red points and lines represent data before 2020. Blue points and lines represent data since 2020. Gray lines and shaded regions represent the mean seasonal patterns and corresponding 95% confidence intervals around the mean. Mean seasonal patterns were calculated by aggregating cases before 2020 into 52 weekly bins and taking the average in each week. Cases were scaled to account for changes in testing patterns (Materials and Methods).

31 Even though more than five years have passed since the emergence of SARS-CoV-
 32 2, we still observe persistent changes in pathogen dynamics following the pandemic

33 NPIs: for example, compared to pre-pandemic, seasonal patterns, human metapneu-
34 movirus in Korea seem to circulate at lower levels, whereas RSV in Korea seem to
35 exhibit different seasonality (Figure 1). These observations suggest a possibility for
36 a fundamental change in pathogen dynamics following the pandemic NPIs, which
37 can be driven by permanent shift in either human behavior or population-level im-
38 munity [7, 8]. The possibility of a long-lasting impact of the pandemic NPIs pose an
39 important question for future infectious disease dynamics: can we predict whether
40 and when other respiratory pathogens will eventually return to their pre-pandemic
41 dynamics? *[SWP: You suggested: I would say something about the dynamics of
42 these pathogens not being well understood, but I've since rewritten the most of intro
43 and I'm not sure where I would fit this. If you have any suggestions, let me know...]*

44 So far, the majority of epidemiological analyses of respiratory pathogens in the
45 context of the pandemic NPIs have focused on characterizing the timing of rebound
46 [1, 9, 5]. Instead, we seek to characterize how fast a pathogen returns to its pre-
47 pandemic dynamics. These two concepts have subtle but important differences: for
48 example, it took more than 3 years for human metapneumovirus to rebound in Hong
49 Kong but the observed epidemic patterns in 2024 are similar to pre-pandemic seasonal
50 means, suggesting a rapid return to pre-pandemic dynamics following a perturbation
51 (Figure 1). Measuring this rate of return is particularly useful because it allows us
52 to quantify the ecological resilience of a host-pathogen system [10, 11, 12, 13].

53 In this study, we lay out theoretical and statistical approaches to characterizing
54 the resilience of a host-pathogen system based on how fast the system recovers from
55 perturbation. We begin by laying out a few representative scenarios that capture the
56 potential impact of NPIs on endemic pathogen dynamics and illustrate how resilience
57 can be measured by comparing the pre- and post-pandemic dynamics of susceptible
58 and infected hosts. In practice, information on susceptible hosts is often unavail-
59 able, making this theoretical approach infeasible. Instead, we utilize a mathematical
60 technique to reconstruct empirical attractors from the data [14], which allows us to
61 measure the rate at which the host-pathogen system approaches this empirical attrac-
62 tor after a perturbation; this rate corresponds to the resilience of the host-pathogen
63 system. We use this method to analyze pathogen surveillance data for respiratory
64 and non-respiratory pathogens from Canada, Hong Kong, Korea, and US. Finally,
65 we show that susceptible host dynamics explain variation in pathogen resilience.

66 Conceptual introduction to pathogen resilience

67 In classical ecological literature, resilience of an ecological system is measured by
68 the rate at which the system returns to its reference state following a perturbation
69 [10, 11, 12, 13]. This rate corresponds to the largest real part of the eigenvalues of
70 the linearized system near equilibrium—here, we refer to this value as the *intrinsic*
71 resilience of the system, which represents the expected rate of return from perturbed
72 states. In practice, we rarely know the true model describing population-level dy-

73 namics of common respiratory pathogens, limiting our ability to infer the intrinsic
74 resilience of a system. Instead, we can still measure the *empirical* resilience of a
75 host-pathogen system by looking at how fast the system returns to the pre-pandemic,
76 endemic dynamics after interventions are lifted.

77 As an example, we begin with a simple Susceptible-Infected-Recovered-Susceptible
78 (SIRS) model with seasonally forced transmission and demography (i.e., birth and
79 death). The SIRS model is the simplest model that allows for waning of immunity
80 and is commonly used for modeling the dynamics of respiratory pathogens [15]. First,
81 consider an intervention that reduce transmission by 50% for 6 months starting in
82 2020, which causes epidemic patterns to deviate from its original stable annual cycle
83 for a short period of time and eventually come back (Figure 2A). To measure the
84 resilience of this system empirically, we first need to be able to measure the dis-
85 tance from its pre-pandemic attractor. There are many ways we can measure the
86 distance from the attractor, but for illustrative purposes, we choose one of the most
87 parsimonious approach: that is, we look at how the susceptible (S) and infected (I)
88 populations change over time and measure the distance on the SI phase plane (Figure
89 2B). In this simple case, the locally estimated scatterplot smoothing (LOESS) fit in-
90 dicates that the distance from the attractor decreases exponentially (linearly on a log
91 scale) on average (Figure 2C). Furthermore, the overall rate of return approximates
92 the intrinsic resilience of the seasonally unforced system (Figure 2C).

93 Alternatively, NPIs can have a lasting impact on the pathogen dynamics; as an
94 example, we consider a scenario in which a 10% reduction in transmission persists
95 even after the NPIs are lifted (Figure 2D–F). In such cases in practice, we can-
96 not know whether the pathogen will return to its original cycle or a different cycle
97 until many years have passed, and we cannot measure the distance to the new un-
98 known attractor that the system might eventually approach. Nonetheless, we can
99 still measure the distance from the pre-pandemic attractor and ask how the distance
100 changes over time (Figure 2E). The LOESS fit suggests that the distance from the
101 pre-pandemic attractor will initially decrease exponentially on average (equivalently,
102 linearly on a log scale) and eventually plateau (Figure 2F). Here, a permanent 10%
103 reduction in transmission rate slows the system, which causes the distance from the
104 pre-pandemic attractor initially to decrease at a slower rate (Figure 2F) than it would
105 have otherwise (Figure 2C) before plateauing at a fixed distance between the two
106 attractors. This example shows that resilience is not necessarily an intrinsic prop-
107 erty of a specific pathogen. Instead, pathogen resilience is a property of a specific
108 attractor that a host-pathogen system approaches, which depends on both pathogen
109 and host characteristics.

110 Finally, transient phenomena can further complicate the picture (Figure 2G–I).
111 For example, a stage-structured model initially exhibits a stable annual cycle, but
112 perturbations from a 10% reduction in transmission for 6 months cause the epidemic
113 to shift to biennial cycles (Figure 2G). The system eventually approaches the original
114 pre-pandemic attractor (Figure 2H), suggesting that this biennial cycle is a transient
115 phenomenon. The LOESS fit indicates that the distance from the attractor initially

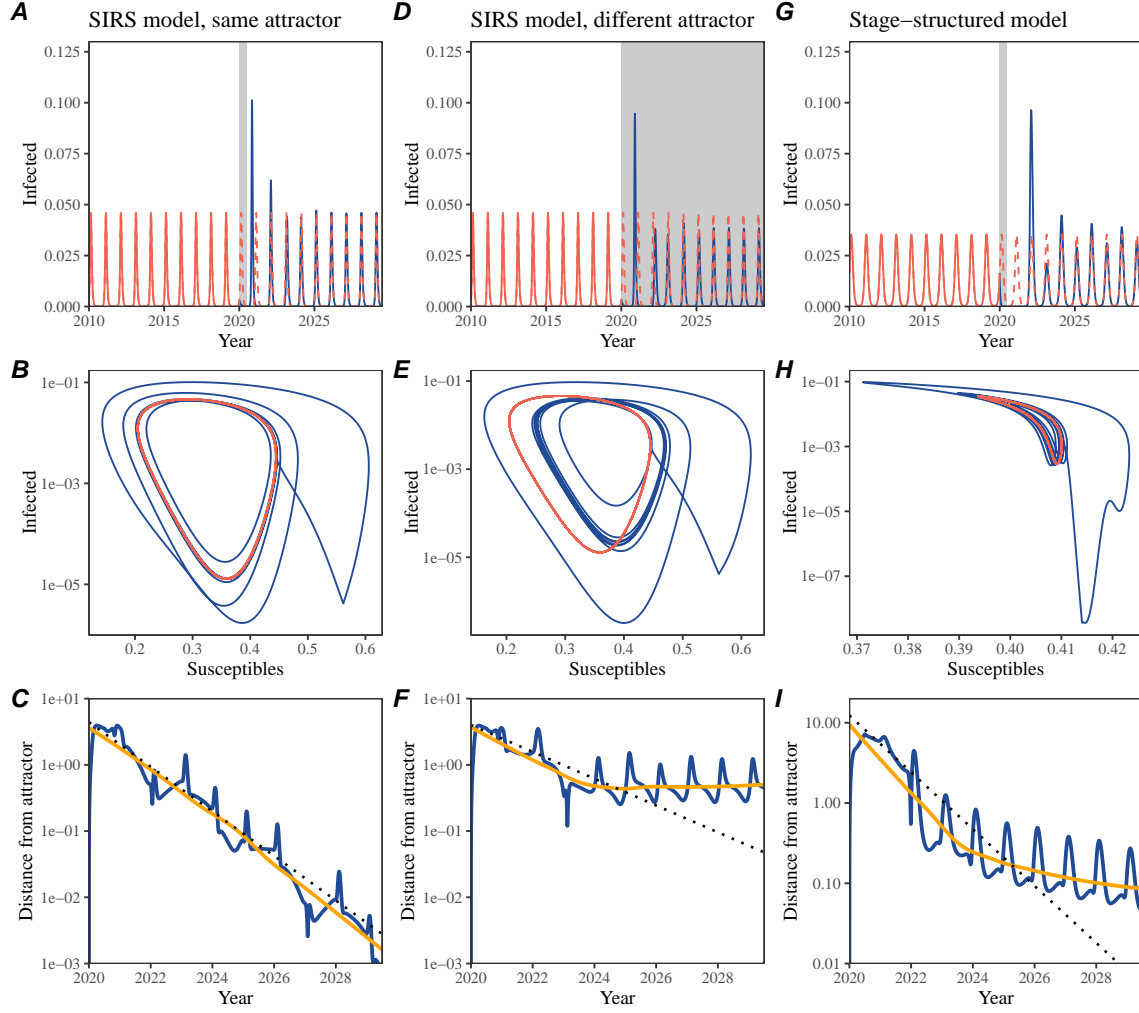


Figure 2: A simple method to measure pathogen resilience following NPIs across different scenarios. (A, D, G) Simulated epidemic trajectories across various models. Red and blue solid lines represent epidemic dynamics before and after interventions are introduced, respectively. Red dashed lines represent counterfactual epidemic dynamics in the absence of interventions. Gray regions indicate the duration of interventions. (B, E, H) Phase plane representation of the time series in panels A, D, and G alongside the corresponding susceptible host dynamics. Red and blue solid lines represent epidemic trajectories on an SI phase plane before and after interventions are introduced, respectively. (C, F, I) Changes in logged distance from the attractor over time. Blue lines represent the logged distance from the attractor. Orange lines represent the locally estimated scatterplot smoothing (LOESS) fits to the logged distance from the attractor. Dotted lines show the intrinsic resilience of the seasonally unforced system.

116 decreases exponentially at a rate that is consistent with the intrinsic resilience of

117 the seasonally unforced stage-structured system, but the rate of decrease decelerates
118 with the damped oscillations (Figure 2I). This behavior is also referred to as a ghost
119 attractor, which causes long transient dynamics and slow transitions [16]. Strong
120 seasonal forcing in transmission can also lead to transient phenomena for a simple
121 SIRS model, causing a slow return to pre-perturbation dynamics (Supplementary
122 Figure S1).

123 This empirical approach allows us to measure the resilience of a two-strain host-
124 pathogen system even when we have incomplete observation of the infection dynam-
125 ics. Simulations from a simple two-strain system illustrate that separate analyses of
126 individual strain dynamics (e.g., RSV A vs B) and a joint analysis of total infections
127 (e.g., total RSV infections) yield identical resilience estimates (Supplementary Fig-
128 ure S2, 3). This is expected because the dynamics of two strains (or two pathogens)
129 around the attractor in a coupled system are described by the same set of eigen-
130 values and eigenvectors, meaning that both strains should exhibit identical rates of
131 returns following a perturbation. Analogous to a single system, strong seasonal forc-
132 ing in transmission can cause the system to slow down through transient phenomena
133 (Supplementary Figure S4).

134 These observations indicate three possibilities. First, we can directly estimate the
135 empirical resilience of a host-pathogen system by measuring the rate at which the
136 system approaches an attractor, provided that we have a way to quantify the distance
137 from the attractor. The empirical approach to estimating pathogen resilience is
138 particularly convenient because it does not require us to know the true underlying
139 model; estimating the intrinsic resilience from fitting misspecified models can lead
140 to biased estimates (Supplementary Figure S5). Second, resilience estimates allow
141 us to make phenomenological predictions about the dynamics of a host-pathogen
142 system following a perturbation. Assuming that the distance from the attractor will
143 decrease exponentially over time, we can obtain a ballpark estimate for when the
144 system will reach an attractor; this prediction necessarily assumes that there won't
145 be permanent changes in pathogen dynamics (Figure 2F) or a long-term transient
146 phenomenon (Figure 2I). Finally, a change in the rate of an exponential decrease in
147 the distance from the attractor can provide information about whether the system
148 has reached an alternative attractor, or a ghost attractor, that is different from the
149 original, pre-pandemic attractor. These alternative attractors may reflect continued
150 perturbations from permanent changes in transmission patterns as well as changes in
151 immune landscapes. There will be periods of time when it is difficult to tell whether
152 pathogen dynamics are still diverging from its original attractor or have begun to
153 converge to an attractor; now that several years have passed since NPIs have been
154 lifted, we expect many respiratory pathogens to have had sufficient time to begin
155 returning to their post-NPI attractors.

156 **Inferring pathogen resilience from real data**

157 Based on these observations, we now lay out our approach to estimating pathogen
158 resilience from real data (Figure 3). We then test this approach against simulations
159 and apply it to real data.

160 So far, we focused on simple examples that assume a constant transmission re-
161 duction. However, in practice, the impact of NPIs on pathogen transmission is likely
162 more complex (Figure 3A), reflecting introduction and relaxation of various NPI
163 strategies. In some cases, strong NPIs can even lead to a local fadeout, requiring im-
164 migration from another location for epidemic re-emergence. These complexities can
165 lead to longer delays between the introduction of NPIs and pathogen re-emergence as
166 well as temporal variation in outbreak sizes (Figure 3B): in this example, continued
167 transmission reduction from NPIs limits the size of the first outbreak in 2021 fol-
168 lowing the emergence, allowing for a larger outbreak in 2022 when NPIs are further
169 relaxed.

170 Previously, we relied on the dynamics of susceptible and infected hosts to com-
171 pute the distance from the attractor (Figure 2), but information on susceptible hosts
172 is rarely available in practice. In addition, uncertainties in case counts due to obser-
173 vation error as well as multiannual cycles in the observed epidemic dynamics (e.g.,
174 adenovirus circulation patterns in Hong Kong and Korea) add challenges to defin-
175 ing pre-pandemic attractors, which limits our ability to measure the distance from
176 the attractor. To address these challenges, we can reconstruct an empirical attrac-
177 tor by utilizing Takens' theorem [14], which states that an attractor of a nonlinear
178 multidimensional system can be mapped onto a delayed embedding (Materials and
179 Methods). For example, we can use delayed logged values of pre-pandemic cases $C(t)$
180 (Figure 3C) to reconstruct the attractor:

$$\langle \log(C(t) + 1), \log(C(t - \tau) + 1), \dots, \log(C(t - (M - 1)\tau) + 1) \rangle, \quad (1)$$

181 where the delay τ and embedding dimension M are determined based on autocor-
182 relations and false nearest neighbors, respectively [17, 18]. We can then apply the
183 same delay and embedding dimensions to the entire time series to determine the
184 position on a multi-dimensional state space (Figure 3D), which allows us to mea-
185 sure the nearest neighbor distance between the current state of the system and the
186 empirical pre-pandemic attractor (Figure 3E). In theory, we can now quantify how
187 fast this distance decreases by fitting a linear regression on a log scale, where the
188 slope of the linear regression corresponds to pathogen resilience. However, resulting
189 estimates of pathogen resilience can be sensitive to choices about embedding delays
190 and dimensions; for example, using longer delays and higher dimensions tends to
191 smooth out temporal variations in the distance from the attractor (Supplementary
192 Figure S6).

193 Complex changes in the distance from the attractor suggest that estimating
194 pathogen resilience from linear regression will be particularly sensitive to our choice
195 of fitting windows for the regression (Figure 3E). Therefore, before we tried estimat-

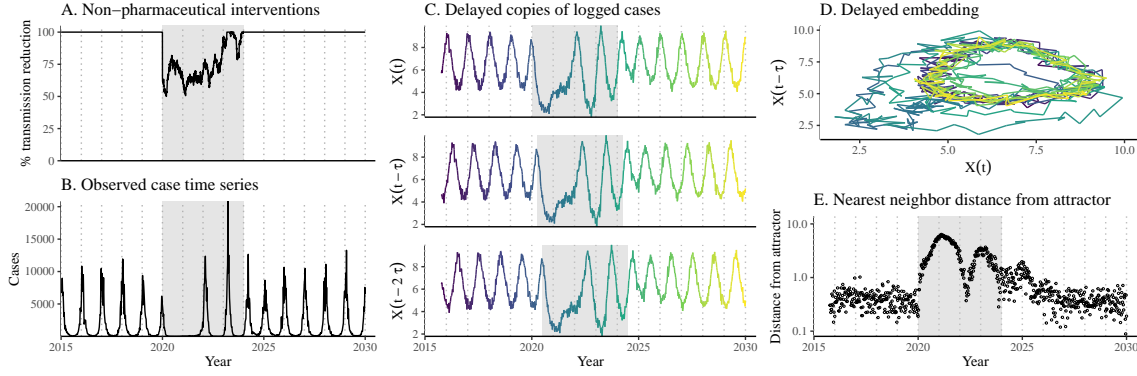


Figure 3: **A schematic diagram explaining the inference of pathogen resilience from synthetic data.** (A) A realistic example of simulated NPIs, represented by a relative reduction in transmission. (B) The impact of the synthetic NPI on epidemic dynamics simulated using a SIRS model with demographic stochasticity. (C) Generating delayed copies of the logged time series allows us to obtain an embedding. (D) Two dimensional representation of an embedding. (E) Delayed embedding allows us to calculate the nearest neighbor distance from the empirical attractor, which is determined based on the pre-pandemic time series. This distance time series can be used to infer pathogen resilience after choosing an appropriate window for linear regression.

ing resilience from real data, we explored an automated window selection criterion for linear regression and test it against randomized, stochastic simulations across a wide range of realistic NPI shape; in doing so, we also explored optimal choices for embedding dimensions and evaluated our choices for fitting window parameters and embedding dimensions by quantifying correlation coefficients between the estimated resilience and the intrinsic resilience of a seasonally unforced system (Materials and Methods). Overall, we find large variation in estimation performances with correlation coefficient ranging from 0.21 to 0.61 (Supplementary Figure S7). In almost all cases, the automated window selection approach outperformed a naive approach that uses the entire time series, starting from the peak distance (Supplementary Figure S7).

Based on the best performing window selection criteria and embedding dimension, we applied this approach to pathogen surveillance data presented in Figure 1 (Materials and Methods). For each time series, we applied Takens' theorem independently to reconstruct the empirical attractor and obtained the corresponding time series of distances from attractors (Supplementary Figure S8). Then, we use the automated window selection criterion to fit a linear regression and estimate the empirical resilience for each pathogen in each country (Supplementary Figure S8); the window selection criterion gave poor regression window for three cases (norovirus in Hong Kong and Korea and Rhinovirus/Enterovirus in the US), leading to unrealistically low resilience estimates, and so we used ad-hoc regression windows instead

217 (Supplementary Figure S9; Materials and Methods).

218 For all pathogens we consider, resilience estimates fall between 0.4/year and
219 1.8/year (Figure 4A). We estimate the mean resilience of common respiratory pathogens
220 to be 0.99/year (95% CI: 0.80/year–1.18/year). As a reference, this is \approx 7.5 times
221 higher than the intrinsic resilience of pre-vaccination measles in England and Wales
222 (\approx 0.13/year). Finally, resilience estimates for norovirus are comparable to those of
223 common respiratory pathogens: 1.44/year (95%CI: 1.01/year–1.87/year) for Hong
224 Kong and 1.07/year (95%CI: 0.86/year–1.29/year) for Korea. Based on a simple
225 ANOVA test, we do not find significant differences in resilience estimates across
226 countries ($p = 0.25$) or pathogens ($p = 0.68$).

227 [SWP: You suggested “I think we probably need to spell out a bit more that
228 long-term changes in the transmission rate (or some other parameter) mean the at-
229 tractor is permanently different and the distance should remain nonzero” and I think
230 we’ve done that enough early on with current revisions so I don’t feel like we need
231 to do it again here. Let me know what you think.] Using resilience estimates, we
232 predicted when each pathogen would hypothetically return to their pre-pandemic
233 dynamics, assuming no long-term change in the attractor. Specifically, we extend
234 our linear regression fits to distance-from-attractor time series and ask when the pre-
235 dicted regression line will cross a threshold value; since we relied on nearest neighbor
236 distances, pre-pandemic distances are always greater than zero (Figure 3E), meaning
237 that we can use the mean of pre-pandemic distances as our threshold.

238 We predict that a return to pre-pandemic cycles would be imminent for most
239 pathogens (Figure 4B). In particular, we predict that 12 out of 23 pathogens should
240 have already returned before the end of 2024. For almost all pathogens that are
241 predicted to have returned already, the observed epidemic dynamics show clear con-
242 vergence towards their pre-NPI seasonal averages, confirming our predictions (Figure
243 4C). However, there are a few exceptions, including norovirus in Hong Kong and Rhi-
244 novirus/Enterovirus in the US, where the observed epidemic dynamics in 2024 exhibit
245 clear deviation from their pre-NPI seasonal averages (Figure 4C). These observations
246 suggest a possibility that some common respiratory pathogens may have converged
247 to different attractors or are still exhibiting non-equilibrium dynamics. In contrast,
248 pathogens that are predicted to have not returned yet also show clear differences
249 from their pre-NPI seasonal averages; as many of these pathogens are predicted to
250 return in 2025–2026, we may be able to test these predictions in near future (Sup-
251 plementary Figure S10). Our reconstructions of distance time series and estimates
252 of pathogen resilience and expected return time are generally robust to choices of
253 embedding dimensions (Supplementary Figure S11–12).

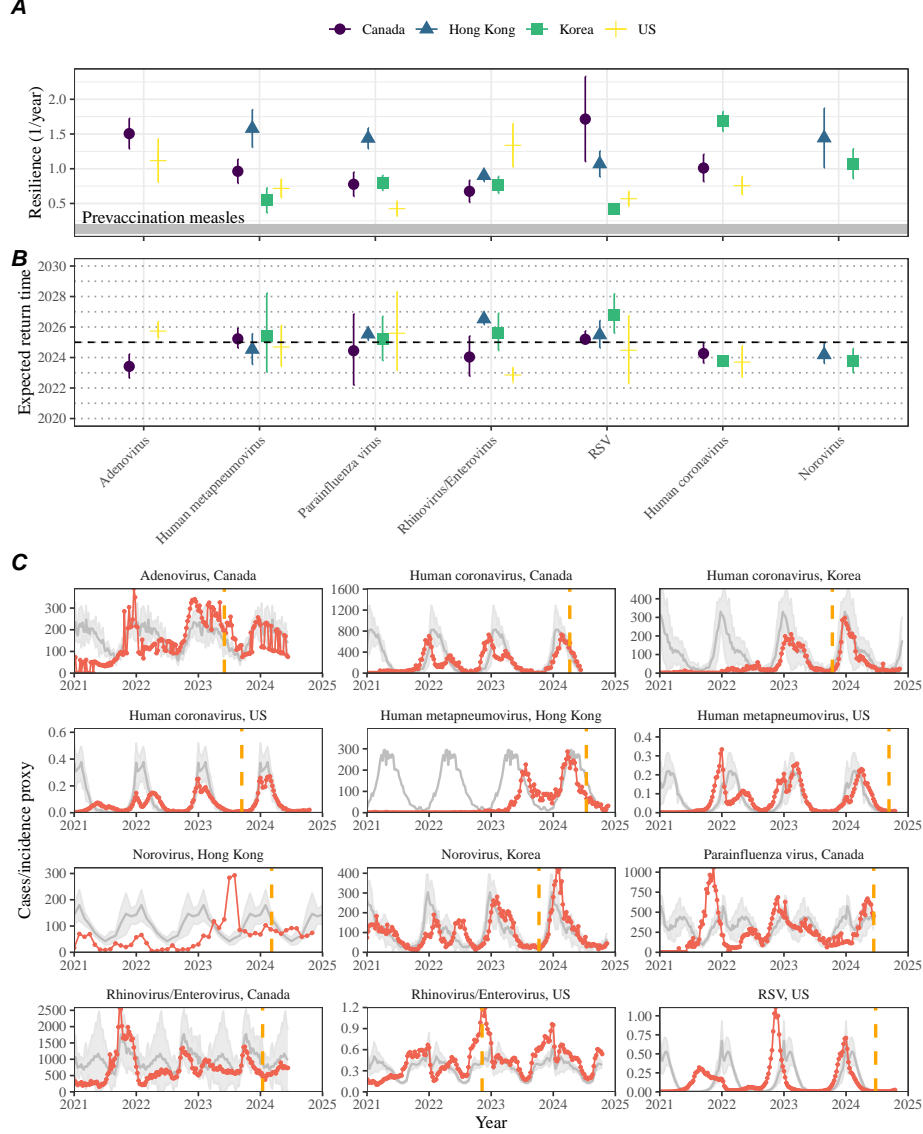


Figure 4: Summary of resilience estimates and predictions for return time. (A) Estimated pathogen resilience. The gray horizontal line represents the intrinsic resilience of pre-vaccination measles dynamics. (B) Predicted timing of when each pathogen will return to their pre-pandemic cycles. The dashed line in panel B indicates the end of 2024 (current observation time). Error bars represent 95% confidence intervals. (C) Observed dynamics for pathogen that are predicted to have returned before the end of 2024. Red points and lines represent data before 2020. Gray lines and shaded regions represent the mean seasonal patterns and corresponding 95% confidence intervals around the mean, previously shown in Figure 1. Orange vertical lines represent the predicted timing of return.

254 **Susceptible host dynamics explain variation in pathogen
255 resilience**

256 So far, we focused on quantifying pathogen resilience from the observed patterns of
257 pathogen re-emergence following NPIs. But what factors determine how resilient a
258 host-pathogen system is? Here, we use the SIRS model to show that susceptible host
259 dynamics are the key determinants of pathogen resilience. To do so, we vary the
260 basic reproduction number \mathcal{R}_0 , which represents the average number of secondary
261 infections caused by a newly infected individual in a fully susceptible population,
262 and the duration of immunity and compute intrinsic resilience for each parameter.

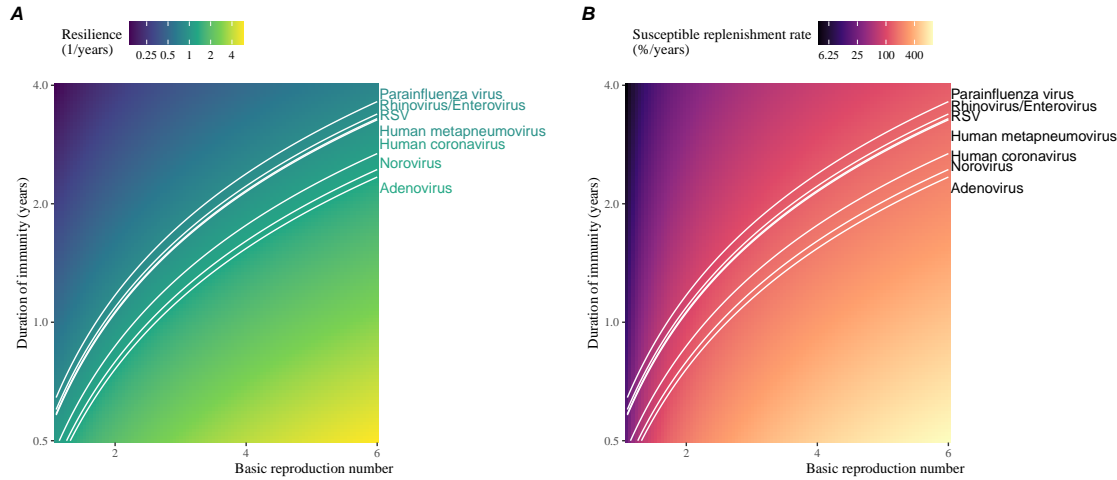


Figure 5: **Linking pathogen resilience to epidemiological parameters and susceptible host dynamics.** (A) The heat map represents intrinsic resilience as a function of the basic reproduction number \mathcal{R}_0 and the duration of immunity. (B) The heat map represents per-capita susceptible replenishment rate as a function of the basic reproduction number \mathcal{R}_0 and the duration of immunity. The standard SIRS model is used to compute intrinsic resilience and per-capita susceptible replenishment rate. Lines correspond to a set of parameters that are consistent with mean resilience estimates for each pathogen. Pathogens are ranked based on their mean resilience estimates, averaged across different countries.

263 We find an increase in \mathcal{R}_0 and a decrease in duration of immunity correspond
264 to an increase in pathogen resilience (Figure 5A). These variations can be under-
265 stood in terms of the susceptible host dynamics, where faster per-capita susceptible
266 replenishment rate causes the system to be more resilient (Figure 5B). This rate can
267 be expressed as a ratio between absolute rate at which new susceptibles enter the
268 population and the equilibrium number of susceptible individuals in the population,
269 \bar{S} . Therefore, both higher \mathcal{R}_0 and shorter duration of immunity can drive faster
270 per-capita susceptible replenishment rate (Figure 5B), especially because higher \mathcal{R}_0

271 leads to lower \bar{S} .

272 We can also rank different pathogens based on the average values of empirical
273 resilience computed previously, which allows us to determine a set of parameters that
274 are consistent with the estimated resilience (Figure 5A). Across all pathogens we
275 consider, except for bocavirus and norovirus, we estimate that the average duration
276 of immunity is likely to be short (< 4 years) across a plausible range of \mathcal{R}_0 (< 6).
277 These rankings further allow us to map each pathogen onto a set of SIRS parameters
278 that are consistent with its empirical resilience (Figure 5A) and obtain a plausible
279 range of susceptible replenishment rates for each pathogen (Figure 5B). However, we
280 note that there is no one-to-one correspondence between susceptible replenishment
281 rates and pathogen resilience, leading to a wide uncertainty in the estimates for
282 susceptible replenishment rates (Figure 5B).

283 **Pathogen resilience determines sensitivity to stochastic perturbations**

285 Beyond the pandemic NPIs, we expect host-pathogen systems to experience con-
286 tinued perturbations of varying degrees from changes in epidemiological conditions,
287 such as human behavior, climate, and viral evolution. These perturbations can also
288 arise from demographic stochasticity, which is inherent to any ecological systems.
289 Here, we use a seasonally unforced SIRS model with birth/death to explore how re-
290 silience of a host-pathogen system determines the sensitivity to perturbations caused
291 by demographic stochasticity (Materials and Methods).

292 We find that resilience of a host-pathogen system determines the amount of devia-
293 tion from the deterministic trajectory caused by demographic stochasticity, with less
294 resilient systems experiencing larger deviations (Figure 6). Notably, less resilience
295 systems also exhibit slower epidemic cycles; the periodicity of this epidemic cycle
296 matches those predicted by the intrinsic periodicity of the system (Supplementary
297 Figure S13). These conclusions are robust for the seasonally forced SIRS model
298 (Supplementary Figure S14). However, we note that resilience is not the only factor
299 that determines sensitivity to stochastic perturbations.

300 **Discussion**

301 The pandemic NPIs have caused major disruptions to circulation patterns of both
302 respiratory and non-respiratory pathogens, adding challenges to predicting their fu-
303 ture dynamics [1, 2, 3, 4]. However, these NPIs offer large-scale natural experiments
304 for understanding how different pathogens respond to perturbations. In this study,
305 we show that pathogen re-emergence patterns following NPIs can be characterized
306 through the lens of ecological resilience. We show that variation in pathogen resilience
307 can be explained by the differences in susceptible host dynamics, where faster replen-

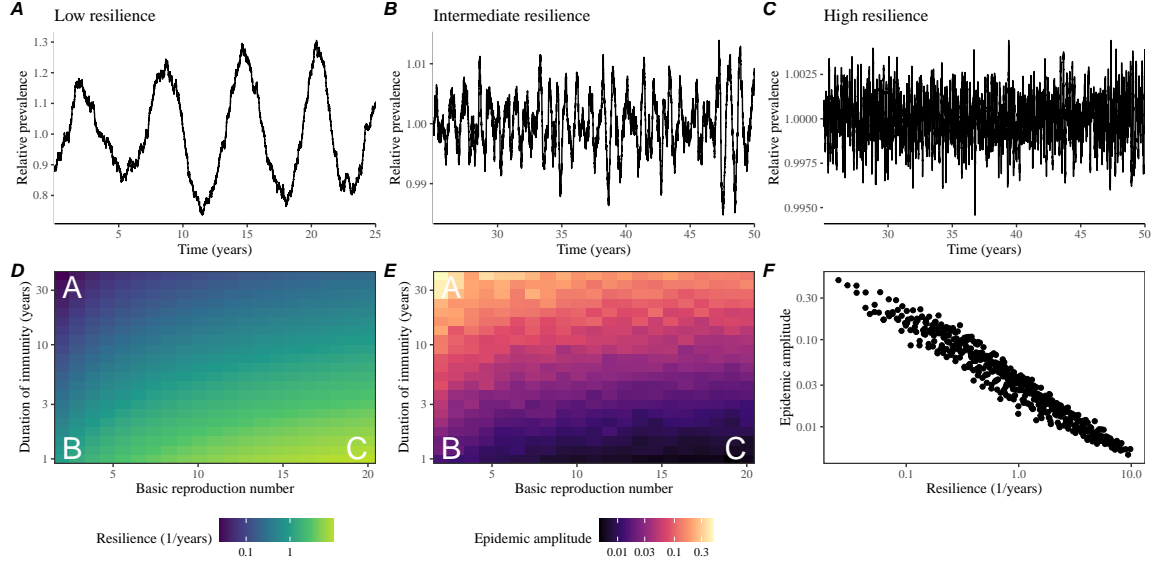


Figure 6: Linking resilience of a host-pathogen system to its sensitivity to stochastic perturbations. (A–C) Epidemic trajectories of a stochastic SIRS model across three different resilience values: low, intermediate, and high. The relative prevalence was calculated by dividing infection prevalence by its mean value. (D) The heat map represents the intrinsic resilience of a system as a function of the basic reproduction number \mathcal{R}_0 and the duration of immunity. (E) The heat map represents the epidemic amplitude as a function of the basic reproduction number \mathcal{R}_0 and the duration of immunity. The epidemic amplitude corresponds to $(\max I - \min I)/(2\bar{I})$, where \bar{I} represents the mean prevalence. (F) The relationship between pathogen resilience and epidemic amplitude.

308 ishment of the susceptible pool corresponds to a more resilient host-pathogen system.
 309 Finally, we show that pathogen resilience also determines the sensitivity to stochastic
 310 perturbations, which in turn determines the persistence of a host-pathogen system.

311 Traditionally, ecological resilience measures how fast a system returns to a ref-
 312 erence state following a perturbation [10, 11, 12, 13]. In the context of respiratory
 313 pathogens, resilience measures how fast epidemics return to their endemic cycles
 314 after NPIs are lifted.

315 We use an attractor reconstruction approach to quantify how distance from the
 316 attractor changes over time for each pathogen [14]. We show that the resilience of
 317 a host-pathogen system can be estimated by fitting a linear regression to a logged
 318 distance-from-attractor time series. Overall, we estimate that the resilience for most
 319 common respiratory pathogens ranges between 0.4/year and 1.8/year, which is 3–14
 320 times more resilient than prevaccination measles, indicating potential challenges in
 321 controlling common respiratory pathogens.

322 Our framework allows us to make phenomenological predictions about when each

323 pathogen will return to their endemic cycles. The ability to predict future epidemic
324 patterns from resilience estimates offers a new paradigm for epidemic forecasting.
325 While this approach cannot predict the exact timing of outbreaks or epidemic pat-
326 terns, it is nonetheless useful for predicting when epidemics will settle down to regular
327 cycles after a large perturbation, such as pandemic NPIs.

328 Our analyses suggest a possibility that several pathogens may have converged
329 to different endemic cycles compared to their pre-pandemic epidemic patterns. Key
330 examples include human metapnuemovirus, RSV, and bocavirus in Korea as well as
331 RSV in Hong Kong. These changes may reflect changes in surveillance or actual shift
332 in the dynamics, caused by permanent changes in behavior or population-level immu-
333 nity. While it seems unlikely that permanent changes in behavior would only affect a
334 few pathogens and not others, we cannot rule out this possibility given heterogeneity
335 in the age of infection across different respiratory pathogens [SWP: CITE]. A shift
336 in population-level immunity is plausible, as the emergence of SARS-CoV-2 and ex-
337 tinction of influenza B/Yamagata likely caused major changes in immune landscapes;
338 interactions among co-circulating pathogens, such as cross immunity between RSV
339 and HMPV [19], may have also contributed to changes in population-level immu-
340 nity. However, we currently do not know how immunity, or lack thereof, from these
341 pathogens would affect infection from other pathogens. Future studies should use
342 detailed mechanistic models, coupled with behavioral and immunological data, to
343 test these hypotheses and better understand post-pandemic dynamics of endemic
344 pathogens.

345 We show that susceptible host dynamics shape pathogen resilience, where faster
346 replenishment of the susceptible population causes the pathogen to be more resilient.
347 For simplicity, we focus on waning immunity and birth as the main drivers of the
348 susceptible host dynamics but other mechanisms can also contribute to the replen-
349 ishment of the susceptible population. In particular, pathogen evolution, especially
350 the emergence of antigenically novel strains, can cause effective waning of immunity
351 in the population; therefore, we hypothesize that faster rates of antigenic evolution
352 can also cause a pathogen to be more resilient. Future studies should explore the
353 relationship between the rate of evolution and resilience for antigenically evolving
354 pathogens.

355 Quantifying pathogen resilience also offers novel approaches to validating population-
356 level epidemiological models. So far, most of model validation in infectious disease
357 ecology is based on the ability of a model to reproduce the observed epidemic dy-
358 namics and to predict future dynamics [20, 19, 21, 22, 23]. However, many models
359 can perform similarly under these criteria. For example, two major RSV models
360 have been proposed to explain biennial epidemic patterns: (1) a stage- and age-
361 structured model that allows disease severity to vary with number of past infections
362 and age of infection [21] and (2) a pathogen-interaction model that accounts for cross
363 immunity between RSV and human metapnuemovirus [19]. Since both models can
364 accurately reproduce the observed epidemic patterns, standard criteria for model
365 validation do not allow us to distinguish between these two models from population-

366 level data alone. Instead, it would be possible to measure the empirical resilience of
367 each model by simulating various perturbations and compare them to estimates of
368 empirical resilience from data, using pandemic NPIs as an opportunity.

369 There are several limitations to our work. First, we did not extensively explore
370 other approaches to reconstructing the attractor. Recent studies showed that more
371 sophisticated approaches, such as using non-uniform embedding, can provide more
372 robust reconstruction for noisy data [18]. In the context of causal inference, choices
373 about embedding can have major impact on the resulting inference [24]. Our re-
374 silience estimates are likely overly confident given a lack of uncertainties in attractor
375 reconstruction as well as the simplicity of our statistical framework. Short pre-
376 pandemic time series also contribute to the crudeness of our estimates. Nonetheless,
377 as illustrated in our sensitivity analyses (Supplementary Figure S6, S10–S12), infer-
378 ences about pathogen resilience in our SIRS model appear to be robust to decisions
379 about embedding lags and dimensions—this is because tracking the rate at which
380 the system approaches the attractor is likely a much simpler problem than making
381 inferences about causal directionality. Our qualitative prediction that common res-
382 piratory pathogens are more resilient than prevaccination measles is also likely to be
383 robust to these predictions, given how rapid many respiratory pathogens returned to
384 their original cycles following pandemic NPIs.

385 Predicting the impact of anthropogenic changes on infectious disease dynamics
386 is a fundamental aim of infectious disease research in a rapidly changing world. Our
387 study illustrates that quantifying pathogen resilience can help us understand how
388 infectious disease pathogens respond to major perturbations caused by NPIs. More
389 broadly, a detailed understanding of the determinants of pathogen resilience may
390 offer unique insights into pathogen persistence and controllability.

391 Materials and Methods

392 Data

393 We gathered time series on respiratory infections from Canada, Hong Kong, Korea,
394 and United States (US). As a reference, we also included time series data on norovirus
395 infections for available countries—in contrast to respiratory pathogens, we expect
396 gastrointestinal viruses, such as norovirus, to be differently affected by pandemic
397 NPIs. For all time series, we rounded every year to 52 weeks by taking the average
398 number of cases and tests between the 52nd and 53rd week. We also rescale all time
399 series to account for changes in testing patterns, which are then used for the actual
400 analysis.

401 Weekly time series of respiratory infection cases in Canada comes from the Res-
402piratory Virus Detection Surveillance System, which collect data from select labo-
403ratories across Canada. We extracted the data from <https://www.canada.ca/en/public-health/services/surveillance/respiratory-virus-detections-canada.html>. To account for an increase in testing from 2013 to 2024, we calculate a 2 year

406 moving average for the number of tests for each pathogen, which we use as a proxy
407 for testing effort. Then, we divide the smoothed testing patterns by the smoothed
408 value at the final week such that the testing effort has a maximum of 1. We then
409 divide weekly cases by the testing effort to obtain a scaled case time series. A similar
410 approach was used earlier for the analysis of RSV time series in the US [21].

411 Weekly time series of respiratory infection cases in Hong Kong comes from the
412 Centre for Health Protection, Department of Health. We extract the data from
413 <https://www.chp.gov.hk/en/statistics/data/10/641/642/2274.html>. We also
414 apply the same scaling procedure to the time series as we did for Canada. For Hong
415 Kong, we only adjust for testing efforts up to the end of 2019 because there was a
416 major reduction in testing for common respiratory pathogens since 2020.

417 Weekly time series of acute respiratory infection cases in Korea comes from Ko-
418 rea Disease Control and Prevention Agency. We extract the data from <https://dportal.kdca.go.kr/pot/is/st/ari.do>. While we do not have information on
419 testing, the reported number of respiratory infections consistently increased from
420 2013 to the end of 2019, which we interpreted as changes in testing patterns. Since
421 we do not have testing numbers, we used the weekly sum of all acute respiratory vi-
422 ral infection cases as a proxy for testing, which were further smoothed with moving
423 averaged and scaled to have a maximum of 1. For Korea, we also only adjust for
424 testing efforts up to the end of 2019.

425 Finally, weekly time series of respiratory infection cases in the US comes from
426 the National Respiratory and Enteric Virus Surveillance System. In the US, there
427 has been a large increase in testing against some respiratory pathogens, especially
428 RSV, which could not be corrected for through simple scaling. Instead, we derive an
429 incidence proxy by multiplying the test positivity with influenza-like illness positivity,
430 which is taken from <https://gis.cdc.gov/grasp/fluview/fluportaldashboard.html>. This method of estimating an incidence proxy has been recently applied in
431 the analysis of seasonal coronaviruses [7] and *Mycoplasma pneumoniae* infections [4].
432 Detailed assumptions and justifications are provided in [25].

435 Estimating pathogen resilience

436 In order to measure pathogen resilience from surveillance data, we first reconstruct
437 the empirical pre-pandemic attractor of the system using Takens' embedding theorem
438 [14]. Specifically, for a given pathogen, we take the pre-pandemic (before 2020)
439 case time series $C(t)$ and reconstruct the attractor using delayed embedding with a
440 uniform delay of τ and dimension M :

$$X_{\tau,m}(t) = \langle \log(C(t) + 1), \log(C(t - \tau) + 1), \dots, \log(C(t - (M - 1)\tau) + 1) \rangle. \quad (2)$$

441 Here, the delay τ is determined by calculating the autocorrelation of the logged pre-
442 pandemic time series and asking when the autocorrelation crosses 0 for the first time
443 [18]; a typical delay for an annual outbreak is around 13 weeks.

444 Then, for a given delay τ , we determine the embedding dimension M using the
 445 false nearest neighbors approach [17, 18]. To do so, we start with an embedding
 446 dimension e and construct a set of points $A_{\tau,e} = \{X_{\tau,e}(t) | t < 2020\}$. Then, for
 447 each point $X_{\tau,e}(t)$, we determine the nearest neighbor from the set $A_{\tau,e}$, which we
 448 denote $X_{\tau,e}(t_{nn})$ for $t \neq t_{nn}$. Then, if the distance between these two points on
 449 $e + 1$ dimension, $D_{\tau,e+1}(t) = \|X_{\tau,e+1}(t_{nn}) - X_{\tau,e+1}(t)\|_2$, is larger than their distance
 450 on e dimension, $D_{\tau,e}(t) = \|X_{\tau,e}(t_{nn}) - X_{\tau,e}(t)\|_2$, these two points are deemed to
 451 be false nearest neighbors; specifically, we use a threshold R for the ratio between
 452 two distances $D_{\tau,e+1}(t)/D_{\tau,e}(t)$ to determine false nearest neighbors. In the main
 453 text, we determine the embedding dimension based on the first dimension without
 454 any false nearest neighbors for $R = 10$. In Supplementary Materials, we impose
 455 $R = 5$ to select for higher dimensions. Once we determine the embedding lag τ
 456 and dimension M , we apply the embedding to the entire time series and calculate
 457 the nearest neighbor distance against the attractor $A_{\tau,M}$ to obtain a time series of
 458 distance from the attractor $D_{\tau,M}(t)$.

459 From a time series of distances from the attractor, we estimate pathogen resilience
 460 by fitting a linear regression to an appropriate window. To automatically select
 461 the fitting window, we begin by smoothing the distance time series using locally
 462 estimated scatterplot smoothing (LOESS) to obtain $\hat{D}_{\tau,M}(t)$, where the smoothing
 463 is performed on a log scale and exponentiated afterwards. Then, we determine
 464 threshold values (T_{start} and T_{end}) for the smoothed distances and choose the fitting
 465 window based on when $\hat{D}_{\tau,M}(t)$ crosses these threshold values for the first time.
 466 These thresholds are determined by first calculating maximum distance,

$$\max \hat{D} = \max \hat{D}_{\tau,M}(t), \quad (3)$$

467 and mean pre-pandemic distance,

$$\hat{D}_{\text{mean}} = \frac{1}{N_{t<2020}} \sum_{t<2020} \hat{D}_{\tau,M}(t), \quad (4)$$

468 as a reference, and then dividing their ratios into 10 equal bins:

$$T_{\text{start}} = \hat{D}_{\text{mean}} \times \left(\frac{\max \hat{D}}{\hat{D}_{\text{mean}}} \right)^{9/10} \quad (5)$$

$$T_{\text{end}} = \hat{D}_{\text{mean}} \times \left(\frac{\max \hat{D}}{\hat{D}_{\text{mean}}} \right)^{1/10} \quad (6)$$

469 This allows us to discard the initial period during which the distance increases (from
 470 the introduction of intervention measures) and the final period during which the
 471 distance plateaus (as the system reaches an attractor). The fitting window is deter-
 472 mined based on when the smoothed distance $\hat{D}_{\tau,M}(t)$ crosses these threshold values
 473 for the first time; then, we fit a linear regression to logged (unsmoothed) distances
 474 $\log D_{\tau,M}(t)$ using that window.

475 **Mathematical modeling**

476 Throughout the paper, we use a series of mathematical models to illustrate the con-
 477 cept of pathogen resilience and to understand the determinants of pathogen resilience.
 478 In general, the intrinsic resilience for a given system is given by the largest real part
 479 of the eigenvalues of the linearized system at endemic equilibrium. Here, we focus on
 480 the SIRS model with demography and present the details of other models in Supple-
 481 mentary Materials. The SIRS (Susceptible-Infected-Recovered-Susceptible) model is
 482 the simplest model that allows for waning of immunity, where recovered (immune)
 483 individuals are assumed to become fully susceptible after an average of $1/\delta$ time pe-
 484 riod. The dynamics of the SIRS model is described by the following set of differential
 485 equations:

$$\frac{dS}{dt} = \mu - \beta(t)SI - \mu S + \delta R \quad (7)$$

$$\frac{dI}{dt} = \beta(t)SI - (\gamma + \mu)I \quad (8)$$

$$\frac{dR}{dt} = \gamma I - (\delta + \mu)R \quad (9)$$

$$(10)$$

486 where μ represents the birth/death rate, $\beta(t)$ represents the time-varying trans-
 487 mission rate, and γ represents the recovery rate. The basic reproduction number
 488 $\mathcal{R}_0(t) = \beta(t)/(\gamma + \mu)$ is defined as the average number of secondary infections that
 489 a single infected individual would cause in a fully susceptible population at time t
 490 and measures the intrinsic transmissibility of a pathogen.

491 When we first introduce the idea of pathogen resilience (Figure 2), we impose
 492 sinusoidal changes to the transmission rate to account for seasonal transmission:

$$\beta(t) = b_1(1 + \theta \cos(2\pi(t - \phi)))\alpha(t), \quad (11)$$

493 where b_1 represents the baseline transmission rate, θ represents the seasonal am-
 494 plitude, and ϕ represents the seasonal offset term. Here, we also introduce an ex-
 495 tra multiplicative term $\alpha(t)$ to account for the impact of pandemic NPIs, where
 496 $\alpha(t) < 1$ indicates transmission reduction. Figure 2A and 2B are generated assum-
 497 ing $b_1 = 3 \times (365/7 + 1/50)/\text{years}$, $\theta = 0.2$, $\phi = 0$, $\mu = 1/50/\text{years}$, $\gamma = 365/7/\text{years}$,
 498 and $\delta = 1/2/\text{years}$. In Figure 2A, we impose a 50% transmission reduction for 6
 499 months from 2020:

$$\alpha(t) = \begin{cases} 0.5 & 2020 \leq t < 2020.5 \\ 1 & \text{otherwise} \end{cases} \quad (12)$$

500 In Figure 2B, we impose a 50% transmission reduction for 6 months from 2020 and
 501 a permanent 10% reduction onward:

$$\alpha(t) = \begin{cases} 1 & t < 2020 \\ 0.5 & 2020 \leq t < 2020.5 \\ 0.9 & 2020.5 \leq t \end{cases} \quad (13)$$

502 In both scenarios, we simulate the SIRS model from the following initial conditions
503 ($S(0) = 1/\mathcal{R}_0$, $I(0) = 1 \times 10^{-6}$, and $R(0) = 1 - S(0) - I(0)$) from 1900 until 2030.

504 To measure the empirical resilience of the SIR model (Figure 2C and 2F), we
505 compute the normalized distance between post-intervention susceptible and logged
506 infected proportions and their corresponding pre-intervention values at the same time
507 of year:

$$\sqrt{\left(\frac{S(t) - S_{\text{pre}}(t)}{\sigma_S}\right)^2 + \left(\frac{\log I(t) - \log I_{\text{pre}}(t)}{\sigma_{\log I}}\right)^2}, \quad (14)$$

508 where σ_S and $\sigma_{\log I}$ represent the standard deviation in the pre-intervention suscep-
509 tible and logged infected proportions. We normalize the differences in susceptible
510 and logged infected proportions to allow both quantities to equally contribute to the
511 changes in distance from the attractor. We used logged prevalence, instead of absolute
512 prevalence, in order to capture epidemic dynamics in deep troughs during the
513 intervention period. In Supplementary Materials, we also compare how the degree
514 of seasonal transmission affects empirical resilience by varying θ from 0 to 0.4; when
515 we assume no seasonality ($\theta = 0$), we do not normalize the distance because the
516 standard deviation of pre-intervention dynamics are zero.

517 Finally, we use the SIRS model to understand how underlying epidemiological
518 parameters affect pathogen resilience and link this relationship to underlying sus-
519 ceptible host dynamics. For the simple SIRS model without seasonal transmission
520 ($\theta = 0$), the intrinsic resilience corresponds to

$$-\frac{\text{Re}(\lambda)}{2} = \frac{\delta + \beta I^* + \mu}{2}. \quad (15)$$

521 Here, I^* represents the prevalence at endemic equilibrium:

$$I^* = \frac{(\delta + \mu)(\beta - (\gamma + \mu))}{\beta(\delta + \gamma + \mu)}. \quad (16)$$

522 The susceptible replenishment rate is given by

$$S_{\text{replenish}} = \frac{\mu + \delta R}{S^*}, \quad (17)$$

523 where $S^* = 1/\mathcal{R}_0$ represents the equilibrium proportion of susceptible individuals.
524 We vary the basic reproduction number \mathcal{R}_0 between 1.1 to 6 and the average duration
525 of immunity $1/\delta$ between 2 to 80 years, and compute these two quantities. In doing
526 so, we fix all other parameters: $\mu = 1/80/\text{years}$ and $\gamma = 365/7/\text{years}$.

527 Data availability

528 Funding

529 **Supplementary Text**

530 **Resilience of a stage-structured system.**

531 In Figure 2G–I, we use a more realistic, stage-structured model to illustrate how
 532 transient phenomena can cause the system to slow down. Specifically, we use the
 533 stage-structured RSV model proposed by [21], which assumes that subsequent rein-
 534 fections cause an individual to become less susceptible and transmissible than previ-
 535 ous infections. The model dynamics can be described as follows:

$$\frac{dM}{dt} = \mu - (\omega + \mu)M \quad (S1)$$

$$\frac{dS_0}{dt} = \omega M - (\lambda(t) + \mu)S_0 \quad (S2)$$

$$\frac{dI_1}{dt} = \lambda(t)S_0 - (\gamma_1 + \mu)I_1 \quad (S3)$$

$$\frac{dS_1}{dt} = \gamma_1 I_1 - (\sigma_1 \lambda(t) + \mu)S_1 \quad (S4)$$

$$\frac{dI_2}{dt} = \sigma_1 \lambda(t)S_1 - (\gamma_2 + \mu)I_2 \quad (S5)$$

$$\frac{dS_2}{dt} = \gamma_2 I_2 - (\sigma_2 \lambda(t) + \mu)S_2 \quad (S6)$$

$$\frac{dI_3}{dt} = \sigma_2 \lambda(t)S_2 - (\gamma_3 + \mu)I_3 \quad (S7)$$

$$\frac{dS_3}{dt} = \gamma_3 I_3 - (\sigma_3 \lambda(t) + \mu)S_3 + \gamma_4 I_4 \quad (S8)$$

$$\frac{dI_4}{dt} = \sigma_3 \lambda(t)S_3 - (\gamma_4 + \mu)I_4 \quad (S9)$$

(S10)

536 where M represents the proportion of individuals who are maternally immune; S_i
 537 represents the proportion of individuals who are susceptible after i prior infections; I_i
 538 represents the proportion of individuals who are currently (re)-infected with their i -th
 539 infection; μ represents the birth and death rates; $1/\omega$ represents the mean duration
 540 of maternal immunity; $1/\gamma_i$ represents the mean duration of infection; $\lambda(t)$ represents
 541 the force of infection; and σ_i represents the reduction in susceptibility for the i -th
 542 reinfection. The force of infection is modeled using a sinusoidal function:

$$\beta(t) = b_1(1 + \theta \cos(2\pi(t - \phi)))\alpha(t) \quad (S11)$$

$$\lambda(t) = \beta(I_1 + \rho_1 I_2 + \rho_2(I_3 + I_4)), \quad (S12)$$

543 where b_1 represents the baseline transmission rate; θ represents the seasonal ampli-
 544 tude; ϕ represents the seasonal offset term; $\alpha(t)$ represents the intervention effect;
 545 and ρ_i represents the impact of immunity on transmission reduction. We use the

546 following parameters to simulate the impact of interventions on epidemic dynam-
 547 ics [21]: $b_1 = 9 \times (365/10 + 1/80)/\text{years}$, $\theta = 0.2$, $\phi = -0.1$, $\omega = 365/112/\text{years}$,
 548 $\gamma_1 = 365/10/\text{years}$, $\gamma_2 = 365/7/\text{years}$, $\gamma_3 = 365/5/\text{years}$, $\sigma_1 = 0.76$, $\sigma_2 = 0.6$,
 549 $\sigma_3 = 0.4$, $\rho_1 = 0.75$, $\rho_2 = 0.51$, and $\mu = 1/80/\text{years}$. We assume a 50% transmission
 550 reduction for 6 months from 2020:

$$\alpha(t) = \begin{cases} 0.5 & 2020 \leq t < 2020.5 \\ 1 & \text{otherwise} \end{cases} \quad (\text{S13})$$

551 The model is simulated from 1900 to 2030 using the following initial conditions:
 552 $M = 0$, $S_0 = 1/\mathcal{R}_0 - I_1$, $I_1 = 1 \times 10^{-6}$, $S_1 = 1 - 1/\mathcal{R}_0$, $I_2 = 0$, $S_2 = 0$, $I_3 = 0$,
 553 $S_3 = 0$, and $I_4 = 0$. For the phase plane analysis (Figure 2H) and distance analysis
 554 (Figure 2I), we rely on the average susceptibility,

$$\bar{S} = S_0 + \sigma_1 S_1 + \sigma_2 S_2 + \sigma_3 S_3, \quad (\text{S14})$$

555 and total prevalence,

$$I_{\text{total}} = I_1 + I_2 + I_3 + I_4. \quad (\text{S15})$$

556 These quantities are used to compute the normalized distance from the attractor, as
 557 described in the main text.

558 Resilience of a multistrain system.

559 We use a simple two-strain model to show that a multistrain host-pathogen system
 560 that is coupled through cross immunity can be described by a single resilience value.
 561 The model dynamics can be described as follows [19]:

$$\frac{dS}{dt} = \mu - \mu S - (\lambda_1 + \lambda_2)S + \rho_1 R_1 + \rho_2 R_2 \quad (\text{S16})$$

$$\frac{dI_1}{dt} = \lambda_1 S - (\gamma_1 + \mu)I_1 \quad (\text{S17})$$

$$\frac{dI_2}{dt} = \lambda_2 S - (\gamma_2 + \mu)I_2 \quad (\text{S18})$$

$$\frac{dR_1}{dt} = \gamma_1 I_1 - \lambda_2 \epsilon_{21} R_1 - \rho_1 R_1 + \rho_2 R - \mu R_1 \quad (\text{S19})$$

$$\frac{dR_2}{dt} = \gamma_2 I_2 - \lambda_1 \epsilon_{12} R_2 - \rho_2 R_2 + \rho_1 R - \mu R_2 \quad (\text{S20})$$

$$\frac{dJ_1}{dt} = \lambda_1 \epsilon_{12} R_2 - (\gamma_1 + \mu)J_1 \quad (\text{S21})$$

$$\frac{dJ_2}{dt} = \lambda_2 \epsilon_{21} R_1 - (\gamma_2 + \mu)J_2 \quad (\text{S22})$$

$$\frac{dR}{dt} = \gamma_1 J_1 + \gamma_2 J_2 - \rho_1 R - \rho_2 R - \mu R \quad (\text{S23})$$

562 where S represents the proportion of individuals who are fully susceptible to infections
 563 by both strains; I_1 represents the proportion of individuals who are infected with strain 1 without prior immunity; I_2 represents the proportion of individuals who are infected with strain 2 without prior immunity; R_1 represents the proportion of individuals who are fully immune against strain 1 and partially susceptible to reinfection by strain 2; R_2 represents the proportion of individuals who are fully immune against strain 2 and partially susceptible to reinfection by strain 1; J_1 represents the proportion of individuals who are infected with strain 1 with prior immunity against strain 2; J_2 represents the proportion of individuals who are infected with strain 2 with prior immunity against strain 1; R represents the proportion of individuals who are immune to infections from both strains; μ represents the birth/death rate; λ_1 and λ_2 represent the force of infection from strains 1 and 2, respectively; ρ_1 and ρ_2 represent the waning immunity rate; γ_1 and γ_2 represent the recovery rate; ϵ_{21} and ϵ_{12} represent the susceptibility to reinfection with strains 2 and 1, respectively, given prior immunity from infection with strains 1 and 2, respectively. The force of infection is modeled as follows:

$$\beta_1 = b_1(1 + \theta_1 \sin(2\pi(t - \phi_1)))\alpha(t) \quad (\text{S24})$$

$$\beta_2 = b_2(1 + \theta_2 \sin(2\pi(t - \phi_2)))\alpha(t) \quad (\text{S25})$$

$$\lambda_1 = \beta_1(I_1 + J_1) \quad (\text{S26})$$

$$\lambda_2 = \beta_2(I_2 + J_2) \quad (\text{S27})$$

578 In Supplementary Figures S2–S4, we assume the following parameters: $b_1 = 2 \times$
 579 $52/\text{years}$, $b_2 = 4 \times 52/\text{years}$, $\phi_1 = \phi_2 = 0$, $\epsilon_{12} = 0.9$, $\epsilon_{21} = 0.5$, $\gamma_1 = \gamma_2 = 52/\text{years}$,
 580 $\rho_1 = \rho_2 = 1/\text{years}$, and $\mu = 1/70/\text{years}$. For all simulations, we assume a 50%
 581 transmission reduction for 6 months from 2020:

$$\alpha(t) = \begin{cases} 0.5 & 2020 \leq t < 2020.5 \\ 1 & \text{otherwise} \end{cases} \quad (\text{S28})$$

582 The seasonal amplitude θ is varied from 0 to 0.4. All simulations were ran from 1900
 583 to 2030 with following initial conditions: $S(0) = 1 - 2 \times 10^{-6}$, $I_1(0) = 1 \times 10^{-6}$,
 584 $I_2(0) = 1 \times 10^{-6}$, $R_1(0) = 0$, $R_2(0) = 0$, $J_1(0) = 0$, $J_2(0) = 0$, and $R(0) = 0$.

585 We consider three scenarios for measuring pathogen resilience: (1) we only have
 586 information about strain 1, (2) we only have information about strain 2, and (3)
 587 we are unable to distinguish between strains. In the first two scenarios (see panels
 588 A–C for strain 1 and panels D–F for strain 2), we consider the dynamics of average
 589 susceptibility for each strain and total prevalence:

$$\bar{S}_1 = S + \epsilon_{12}R_2 \quad (\text{S29})$$

$$\hat{I}_1 = I_1 + J_1 \quad (\text{S30})$$

$$\bar{S}_2 = S + \epsilon_{21}R_1 \quad (\text{S31})$$

$$\hat{I}_2 = I_2 + J_2 \quad (\text{S32})$$

⁵⁹⁰ In the third scenario (panels G–I), we consider the dynamics of total susceptible and
⁵⁹¹ infected populations:

$$\hat{S} = S + R_2 + R_1 \quad (\text{S33})$$

$$\hat{I} = I_1 + J_1 + I_2 + J_2 \quad (\text{S34})$$

⁵⁹² These quantities are used to compute the normalized distance from the attractor, as
⁵⁹³ described in the main text.

⁵⁹⁴ Estimating intrinsic resilience using mechanistic model

⁵⁹⁵ We tested whether we can reliably estimate the intrinsic resilience of a system by fit-
⁵⁹⁶ ting a mechanistic model. Specifically, we simulated case time series from stochastic
⁵⁹⁷ SIRS and two-strain models and fitted a simple, deterministic SIRS model using a
⁵⁹⁸ Bayesian framework.

⁵⁹⁹ We simulated the models in discrete time, incorporating demographic stochastic-
⁶⁰⁰ ity:

$$\beta(t) = \mathcal{R}_0 \left(1 + \theta \cos \left(\frac{2\pi t}{364} \right) \right) \alpha(t)(1 - \exp(-\gamma)) \quad (\text{S35})$$

$$\text{FOI}(t) = \beta(t)I(t - \Delta t)/N \quad (\text{S36})$$

$$B(t) \sim \text{Poisson}(\mu N) \quad (\text{S37})$$

$$\Delta S(t) \sim \text{Binom}(S(t - \Delta t), 1 - \exp(-(\text{FOI}(t) + \mu)\Delta t)) \quad (\text{S38})$$

$$N_{SI}(t) \sim \text{Binom}\left(\Delta S(t), \frac{\text{FOI}(t)}{\text{FOI}(t) + \mu}\right) \quad (\text{S39})$$

$$\Delta I(t) \sim \text{Binom}(I(t - \Delta t), 1 - \exp(-(\gamma + \mu)\Delta t)) \quad (\text{S40})$$

$$N_{IR}(t) \sim \text{Binom}\left(\Delta I(t), \frac{\gamma}{\gamma + \mu}\right) \quad (\text{S41})$$

$$\Delta R(t) \sim \text{Binom}(R(t - \Delta t), 1 - \exp(-(\delta + \mu)\Delta t)) \quad (\text{S42})$$

$$N_{RS}(t) \sim \text{Binom}\left(\Delta R(t), \frac{\delta}{\delta + \mu}\right) \quad (\text{S43})$$

$$S(t) = S(t - \Delta t) + N_{RS}(t) + B(t) - \Delta S(t) \quad (\text{S44})$$

$$I(t) = I(t - \Delta t) + N_{SI}(t) - \Delta I(t) \quad (\text{S45})$$

$$R(t) = R(t - \Delta t) + N_{IR}(t) - \Delta R(t) \quad (\text{S46})$$

⁶⁰¹ where FOI represent the force of infection; N_{ij} represent the number of individuals
⁶⁰² moving from compartment i to j on a given day; and $B(t)$ represents the number
⁶⁰³ of new births. We simulate the model on a daily scale—assuming 364 days in a
⁶⁰⁴ year so that it can be evenly grouped into 52 weeks—with the following parameters:
⁶⁰⁵ $\mathcal{R}_0 = 3$, $\theta = 0.1$, $\gamma = 1/7/\text{days}$, $\delta = 1/(364 \times 2)/\text{days}$, $\mu = 1/(364 \times 50)/\text{days}$, and
⁶⁰⁶ $N = 1 \times 10^8$. The model is simulated from 1900 to 2030 assuming $S(0) = N/3$,

607 $I(0) = 100$, and $R(0) = N - S(0) - I(0)$. The observed incidence from the model is
 608 then simulated as follows:

$$C(t) = \text{Beta-Binom}(N_{SI}(t), \rho, k), \quad (\text{S47})$$

609 where ρ represents the reporting probability and k represents the overdispersion pa-
 610 rameter of beta-binomial distribution. Here, we use the beta-binomial distribution to
 611 account for overdispersion in reporting. We assume $\rho = 0.002$ (i.e., 0.2% probability)
 612 and $k = 1000$.

613 We used an analogous approach for the two-strain model:

$$\beta_1(t) = b_1 \left(1 + \theta_1 \cos \left(\frac{2\pi(t - \phi_1)}{364} \right) \right) \alpha(t) \quad (\text{S48})$$

$$\beta_2(t) = b_2 \left(1 + \theta_2 \cos \left(\frac{2\pi(t - \phi_2)}{364} \right) \right) \alpha(t) \quad (\text{S49})$$

$$\text{FOI}_1(t) = \beta_1(t)(I_1(t - \Delta t) + J_1(t - \Delta t))/N \quad (\text{S50})$$

$$\text{FOI}_2(t) = \beta_2(t)(I_2(t - \Delta t) + J_2(t - \Delta t))/N \quad (\text{S51})$$

$$B(t) \sim \text{Poisson}(\mu N) \quad (\text{S52})$$

$$\Delta S(t) \sim \text{Binom}(S(t - \Delta t), 1 - \exp(-(\text{FOI}_1(t) + \text{FOI}_2(t) + \mu)\Delta t)) \quad (\text{S53})$$

$$N_{SI_1}(t) \sim \text{Binom}\left(\Delta S(t), \frac{\text{FOI}_1(t)}{\text{FOI}_1(t) + \text{FOI}_2(t) + \mu}\right) \quad (\text{S54})$$

$$N_{SI_2}(t) \sim \text{Binom}\left(\Delta S(t), \frac{\text{FOI}_2(t)}{\text{FOI}_1(t) + \text{FOI}_2(t) + \mu}\right) \quad (\text{S55})$$

$$\Delta I_1(t) \sim \text{Binom}(I_1(t - \Delta t), 1 - \exp(-(\gamma_1 + \mu)\Delta t)) \quad (\text{S56})$$

$$N_{I_1 R_1}(t) \sim \text{Binom}\left(\Delta I_1(t), \frac{\gamma_1}{\gamma_1 + \mu}\right) \quad (\text{S57})$$

$$\Delta I_2(t) \sim \text{Binom}(I_2(t - \Delta t), 1 - \exp(-(\gamma_2 + \mu)\Delta t)) \quad (\text{S58})$$

$$N_{I_2 R_2}(t) \sim \text{Binom}\left(\Delta I_2(t), \frac{\gamma_2}{\gamma_2 + \mu}\right) \quad (\text{S59})$$

$$\Delta R_1(t) \sim \text{Binom}(R_1(t - \Delta t), 1 - \exp(-(\epsilon_{21}\text{FOI}_2(t) + \rho_1 + \mu)\Delta t)) \quad (\text{S60})$$

$$N_{R_1 S}(t) \sim \text{Binom}\left(\Delta R_1(t), \frac{\rho_1}{\epsilon_{21}\text{FOI}_2(t) + \rho_1 + \mu}\right) \quad (\text{S61})$$

$$N_{R_1 J_2}(t) \sim \text{Binom}\left(\Delta R_1(t), \frac{\epsilon_{21}\text{FOI}_2(t)}{\epsilon_{21}\text{FOI}_2(t) + \rho_1 + \mu}\right) \quad (\text{S62})$$

$$\Delta R_2(t) \sim \text{Binom}(R_2(t - \Delta t), 1 - \exp(-(\epsilon_{12}\text{FOI}_1(t) + \rho_2 + \mu)\Delta t)) \quad (\text{S63})$$

$$N_{R_2 S}(t) \sim \text{Binom}\left(\Delta R_2(t), \frac{\rho_2}{\epsilon_{12}\text{FOI}_1(t) + \rho_2 + \mu}\right) \quad (\text{S64})$$

$$N_{R_2 J_1}(t) \sim \text{Binom}\left(\Delta R_2(t), \frac{\epsilon_{12}\text{FOI}_1(t)}{\epsilon_{12}\text{FOI}_1(t) + \rho_2 + \mu}\right) \quad (\text{S65})$$

$$\Delta J_1(t) \sim \text{Binom}(J_1(t - \Delta t), 1 - \exp(-(\gamma_1 + \mu)\Delta t)) \quad (\text{S66})$$

$$N_{J_1R}(t) \sim \text{Binom}\left(\Delta J_1(t), \frac{\gamma_1}{\gamma_1 + \mu}\right) \quad (\text{S67})$$

$$\Delta J_2(t) \sim \text{Binom}(J_2(t - \Delta t), 1 - \exp(-(\gamma_2 + \mu)\Delta t)) \quad (\text{S68})$$

$$N_{J_2R}(t) \sim \text{Binom}\left(\Delta J_2(t), \frac{\gamma_2}{\gamma_2 + \mu}\right) \quad (\text{S69})$$

$$\Delta R(t) \sim \text{Binom}(R(t - \Delta t), 1 - \exp(-(\rho_1 + \rho_2 + \mu)\Delta t)) \quad (\text{S70})$$

$$N_{RR_1}(t) \sim \text{Binom}\left(\Delta R(t), \frac{\rho_1}{\rho_1 + \rho_2 + \mu}\right) \quad (\text{S71})$$

$$N_{RR_2}(t) \sim \text{Binom}\left(\Delta R(t), \frac{\rho_2}{\rho_1 + \rho_2 + \mu}\right) \quad (\text{S72})$$

$$S(t) = S(t - \Delta t) - \Delta S(t) + B(t) + N_{R_1S}(t) + N_{R_2S}(t) \quad (\text{S73})$$

$$I_1(t) = I_1(t - \Delta t) - \Delta I_1(t) + N_{SI_1}(t) \quad (\text{S74})$$

$$I_2(t) = I_2(t - \Delta t) - \Delta I_2(t) + N_{SI_2}(t) \quad (\text{S75})$$

$$R_1(t) = R_1(t - \Delta t) - \Delta R_1(t) + N_{I_1R_1}(t) + N_{RR_1}(t) \quad (\text{S76})$$

$$R_2(t) = R_2(t - \Delta t) - \Delta R_2(t) + N_{I_2R_2}(t) + N_{RR_2}(t) \quad (\text{S77})$$

$$J_1(t) = J_1(t - \Delta t) - \Delta J_1(t) + N_{R_2J_1}(t) \quad (\text{S78})$$

$$J_2(t) = J_2(t - \Delta t) - \Delta J_2(t) + N_{R_1J_2}(t) \quad (\text{S79})$$

$$R(t) = R(t - \Delta t) - \Delta R(t) + N_{J_1R}(t) + N_{J_2R}(t) \quad (\text{S80})$$

We simulate the model on a daily scale with previously estimated parameters for the RSV-HMPV interaction [19]: $b_1 = 1.7/\text{weeks}$, $b_2 = 1.95/\text{weeks}$, $\theta_1 = 0.4$, $\theta_2 = 0.3$, $\phi_1 = 0.005 \times 7/364$, $\phi_2 = 4.99 \times 7/364$, $\epsilon_{12} = 0.92$, $\epsilon_{21} = 0.45$, $\gamma_1 = 1/10/\text{days}$, $\gamma_2 = 1/10/\text{days}$, $\rho_1 = 1/364/\text{days}$, $\rho_2 = 1/364/\text{days}$, $\mu = 1/(70 \times 364)/\text{days}$, and $N = 1 \times 10^8$. The model is simulated from 1900 to 2030 assuming $S(0) = N - 200$, $I_1(0) = 100$, $I_2(0) = 100$, $R_1(0) = 0$, $R_2(0) = 0$, $J_1(0) = 0$, $J_2(0) = 0$, and $R(0) = 0$. The observed incidence for each strain is then simulated as follows:

$$C_1(t) = \text{Beta} - \text{Binom}(N_{SI_1}(t) + N_{R_2J_1}, \rho, k), \quad (\text{S81})$$

$$C_2(t) = \text{Beta} - \text{Binom}(N_{SI_2}(t) + N_{R_1J_2}, \rho, k), \quad (\text{S82})$$

where ρ represents the reporting probability and k represents the overdispersion parameter of beta-binomial distribution. We assume $\rho = 0.002$ (i.e., 0.2% probability) and $k = 500$. We also consider the total incidence: $C_{\text{total}}(t) = C_1(t) + C_2(t)$.

For both models, we consider a more realistic challenges in intervention effects $\alpha(t)$ to challenge our ability to estimate the intervention effects. Thus, we assume a 40% transmission reduction for 3 months from March 2020, followed by a 10% transmission reduction for 6 months, 20% transmission reduction for 3 months, and

628 a final return to normal levels:

$$\alpha(t) = \begin{cases} 1 & t < 2020.25 \\ 0.6 & 2020.25 \leq t < 2020.5 \\ 0.9 & 2020.5 \leq t < 2021 \\ 0.8 & 2021 \leq t < 2021.25 \\ 1 & 2021.25 \leq t \end{cases}. \quad (\text{S83})$$

629 For all simulations, we truncate the time series from the beginning of 2014 to the
630 end of 2023 and aggregate them into weekly cases.

631 To infer intrinsic resilience from time series, we fit a simple discrete time, deter-
632 ministic SIRS model [4]:

$$\Delta t = 1 \text{ week} \quad (\text{S84})$$

$$\text{FOI}(t) = \beta(t)(I(t - \Delta t) + \omega)/N \quad (\text{S85})$$

$$\Delta S(t) = [1 - \exp(-(\text{FOI}(t) + \mu)\Delta t)] S(t - \Delta t) \quad (\text{S86})$$

$$N_{SI}(t) = \frac{\text{FOI}(t)\Delta S(t)}{\text{FOI}(t) + \mu} \quad (\text{S87})$$

$$\Delta I(t) = [1 - \exp(-(\gamma + \mu)\Delta t)] I(t - \Delta t) \quad (\text{S88})$$

$$N_{IR}(t) = \frac{\gamma \Delta I(t)}{\gamma + \mu} \quad (\text{S89})$$

$$\Delta R(t) = [1 - \exp(-(\nu + \mu)\Delta t)] R(t - \Delta t) \quad (\text{S90})$$

$$N_{RS}(t) = \frac{\nu \Delta R(t)}{\nu + \mu} \quad (\text{S91})$$

$$S(t) = S(t - \Delta t) + \mu S - \Delta S(t) + N_{RS}(t) \quad (\text{S92})$$

$$I(t) = I(t - \Delta t) - \Delta I(t) + N_{SI}(t) \quad (\text{S93})$$

$$R(t) = R(t - \Delta t) - \Delta R(t) + N_{IR}(t) \quad (\text{S94})$$

633 where we include an extra term ω to account for external infections. Although actual
634 simulations do not include any external infections, we found that including this term
635 generally helped with model convergence in previous analyses [4]. The transmission
636 rate is divided into a seasonal term $\beta_{\text{seas}}(t)$ (repeated every year) and intervention
637 term $\alpha(t)$, which are estimated jointly:

$$\beta(t) = \beta_{\text{seas}}(t)\alpha(t), \quad (\text{S95})$$

638 where $\alpha < 1$ corresponds to reduction in transmission due to intervention effects. To
639 constrain the smoothness of $\beta_{\text{seas}}(t)$, we impose cyclic, random-walk priors:

$$\beta_{\text{seas}}(t) \sim \text{Normal}(\beta_{\text{seas}}(t - 1), \sigma) \quad t = 2 \dots 52 \quad (\text{S96})$$

$$\beta_{\text{seas}}(1) \sim \text{Normal}(\beta_{\text{seas}}(52), \sigma) \quad (\text{S97})$$

640 [SWP: I noticed that I forgot to put a prior on σ so need to re-do this but won't
 641 change the results.] We fix $\alpha(t) = 1$ for all $t < 2020$ and estimate α assuming a
 642 normal prior:

$$\alpha \sim \text{Normal}(1, 0.25). \quad (\text{S98})$$

643 We assume weakly informative priors on ω and ν :

$$\omega \sim \text{Normal}(0, 200) \quad (\text{S99})$$

$$\nu \sim \text{Normal}(104, 26) \quad (\text{S100})$$

644 We assume that the true birth/death rates, population sizes, and recovery rates are
 645 known. We note, however, that assuming $\gamma = 1/\text{week}$ actually corresponds to a
 646 mean simulated infectious period of 1.6 weeks, which is much longer than the true
 647 value; this approximation allows us to test whether we can still robustly estimate the
 648 intrinsic resilience given parameter mis-specification. Initial conditions are estimated
 649 with following priors:

$$S(0) = Ns(0) \quad (\text{S101})$$

$$I(0) = Ni(0) \quad (\text{S102})$$

$$s(0) \sim \text{Uniform}(0, 1) \quad (\text{S103})$$

$$i(0) \sim \text{Half-Normal}(0, 0.001) \quad (\text{S104})$$

650 Finally, the Observation model is specified as follows:

$$\text{Cases}(t) \sim \text{Negative-Binomial}(\rho N_{SI}(t), \phi) \quad (\text{S105})$$

$$\rho \sim \text{Half-Normal}(0, 0.02) \quad (\text{S106})$$

$$\phi \sim \text{Half-Normal}(0, 10) \quad (\text{S107})$$

651 where ρ represents the reporting probability and ϕ represents the negative binomial
 652 overdispersion parameter.

653 The model is fitted to four separate time series: (1) incidence time series from
 654 the SIRS model, (2) incidence time series for strain 1 from the two-strain model,
 655 (3) incidence time series for strain 2 from the two-strain model, and (4) combined
 656 incidence time series for strains 1 and 2 from the two-strain model. The model was
 657 fitted using rstan [26, 27]. The resulting posterior distribution was used to calculate
 658 the intrinsic resilience of the seasonally unforced system with the same parameters;
 659 eigenvalues of the discrete-time SIR model were computed by numerically finding
 660 the equilibrium and calculating the Jacobian matrix.

661 Validations for window-selection criteria

662 We use stochastic SIRS simulations to validate the window-selection criteria that we
 663 use for the linear regression for estimating empirical resilience. For each simulation,
 664 we begin by generating a random intervention $\alpha(t)$ from a random set of parameters.

665 First, we draw the duration of intervention τ_{npi} from a uniform distribution between
 666 0.5 and 3.5 years. Then, we draw independent normal variables z_i of length $\lfloor 364\tau_{\text{npi}} \rfloor$
 667 with a standard deviation of 0.02 and take a reverse cumulative sum to obtain a
 668 realistic shape for the intervention:

$$x_n = 1 + \sum_{i=n}^{\lfloor 364\tau_{\text{npi}} \rfloor} z_i, \quad n = 1, \dots, \lfloor 364\tau_{\text{npi}} \rfloor. \quad (\text{S108})$$

669 We repeat this random generation process until less than 10% of x_n exceeds 1. Then,
 670 we set any values that are above 1 or below 0 as 1 and 0, respectively. Then, we
 671 randomly draw the minimum transmission during intervention α_{\min} from a uniform
 672 distribution between 0.5 and 0.7 and scale x_n to have a minimum of α_{\min} :

$$x_{\text{scale},n} = \alpha_{\min} + (1 - \alpha_{\min}) \times \frac{x_n - \min x_n}{1 - \min x_n}. \quad (\text{S109})$$

673 This allows us to simulate a realistically shaped intervention:

$$\alpha(t) = \begin{cases} 1 & t < 2020 \\ x_{\text{scale},364(t-2020)} & 2020 \leq t < 2020 + \tau_{\text{npi}} \\ 1 & \tau_{\text{npi}} \leq t \end{cases}. \quad (\text{S110})$$

674 Given this intervention function, we draw \mathcal{R}_0 from a uniform distribution between 1.5
 675 and 3 and the mean duration of immunity $1/\delta$ from a uniform distribution between
 676 0.5 and 2. Then, we simulate the stochastic SIRS model from $S(0) = 10^8/\mathcal{R}_0$ and
 677 $I(0) = 100$ from 1990 to 2025 and truncate the time series to 2014–2025; if the
 678 epidemic becomes extinct before the end of simulation, we discard that simulation
 679 and start over from the intervention generation step. We then apply the window
 680 selection criteria described in the main text to compute the empirical resilience and
 681 compare it against the intrinsic resilience of the seasonally unforced system. We also
 682 compare this with the naive approach that uses the entire distance-from-attractor
 683 time series, starting from the maximum distance. We repeat this procedure 500
 684 times and quantify the correlation between empirical and intrinsic resilience estimates
 685 across two approaches.

Supplementary Figures

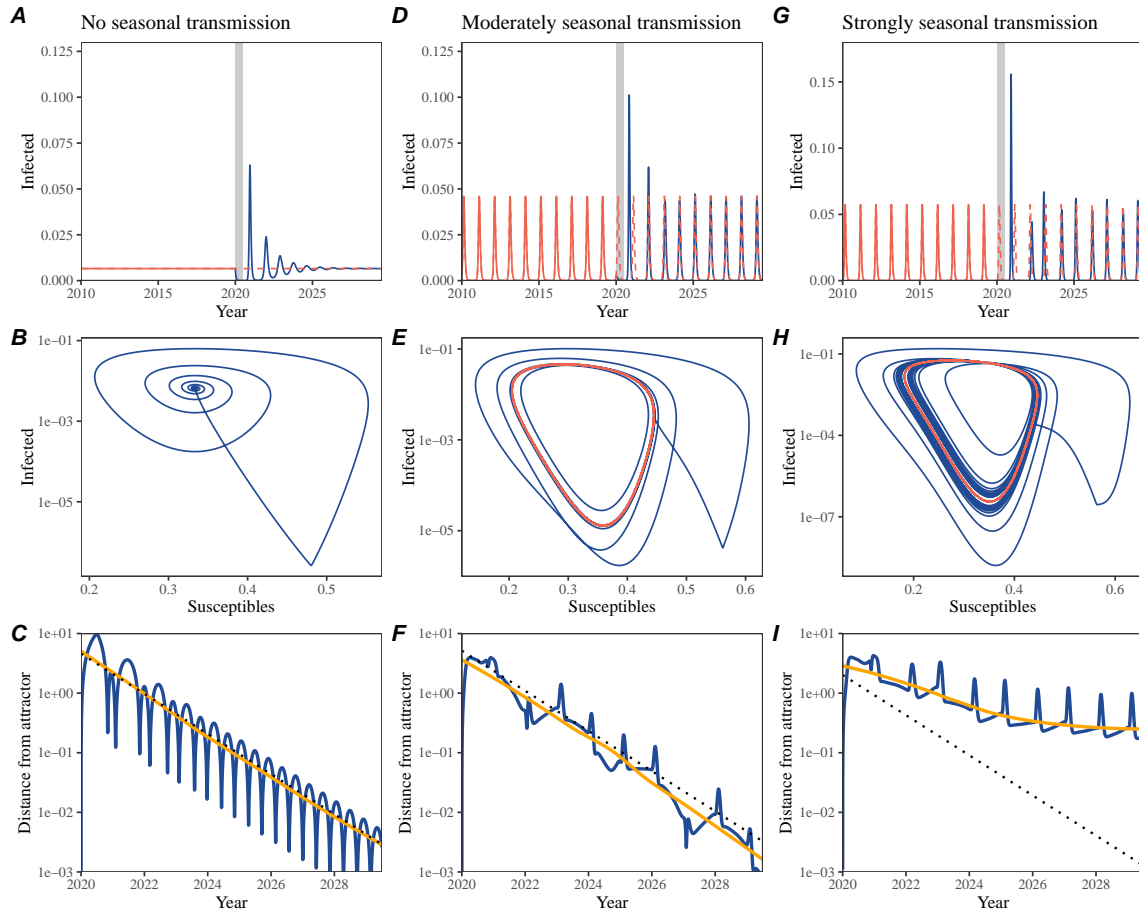


Figure S1: Impact of seasonal transmission on pathogen resilience. (A, D, G) Simulated epidemic trajectories using the SIRS model without seasonal forcing (A), with seasonal forcing of amplitude of 0.2 (D), and with seasonal forcing of amplitude of 0.4 (G). Red and blue solid lines represent epidemic dynamics before and after interventions are introduced, respectively. Red dashed lines represent counterfactual epidemic dynamics in the absence of interventions. Gray regions indicate the duration of interventions. (B, E, H) Phase plane representation of the corresponding model. Red and blue solid lines represent epidemic trajectories on an SI phase plane before and after interventions are introduced, respectively. (C, F, I) Changes in logged distance from the attractor over time. Blue lines represent the logged distance from the attractor. Orange lines represent the locally estimated scatterplot smoothing (LOESS) fits to the logged distance from the attractor. Dotted lines are superimposed as a comparison to have the same slope as the intrinsic resilience of the seasonally unforced system.

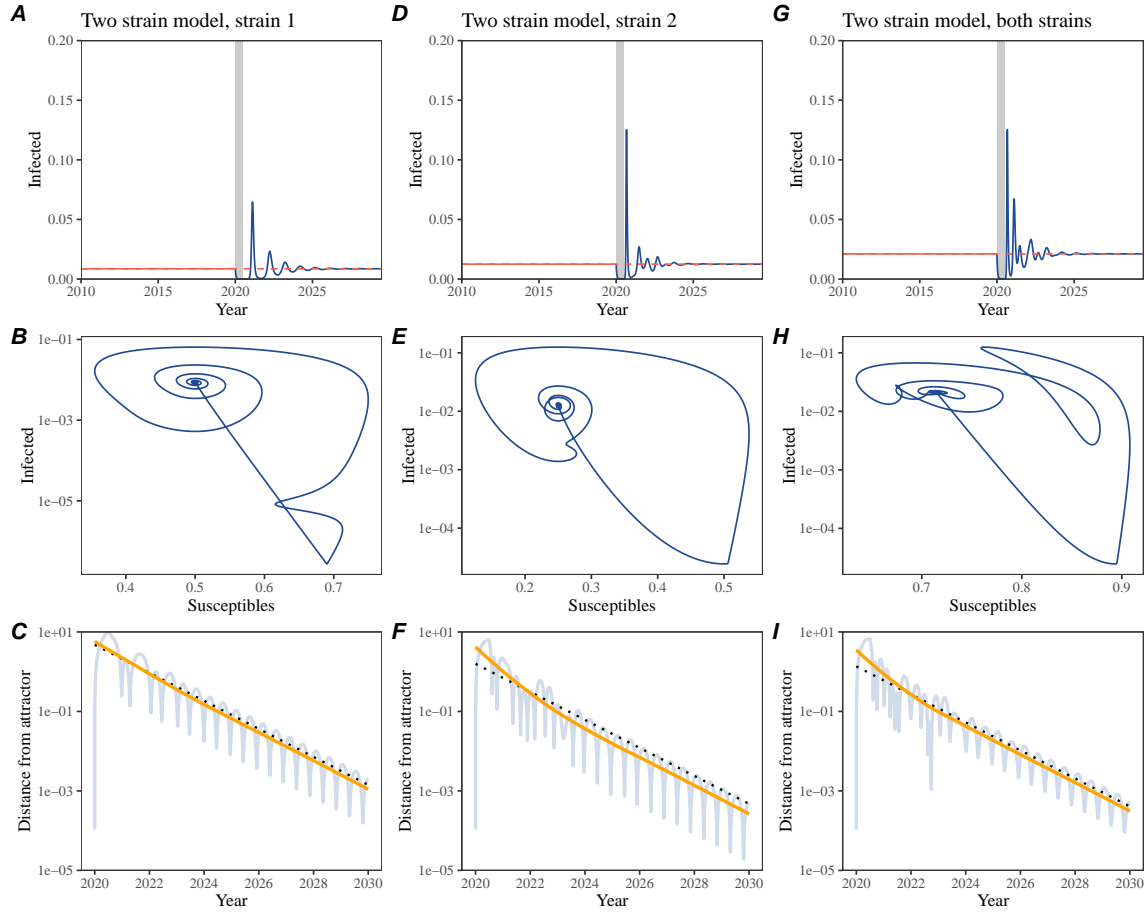


Figure S2: Conceptual framework for measuring pathogen resilience following NPIs for a two-strain system without seasonal forcing. (A, D, G) Simulated epidemic trajectories using a multi-strain system without seasonal forcing. Red and blue solid lines represent epidemic dynamics before and after interventions are introduced, respectively. Red dashed lines represent counterfactual epidemic dynamics in the absence of interventions. Gray regions indicate the duration of interventions. (B, E, H) Phase plane representation of the corresponding model. Blue solid lines represent epidemic trajectories on an SI phase plane before and after interventions are introduced, respectively. (C, F, I) Changes in logged distance from the attractor over time. Blue lines represent the logged distance from the attractor. Orange lines represent the locally estimated scatterplot smoothing (LOESS) fits to the logged distance from the attractor. Dotted lines are superimposed as a comparison to have the same slope as the intrinsic resilience of the seasonally unforced system.

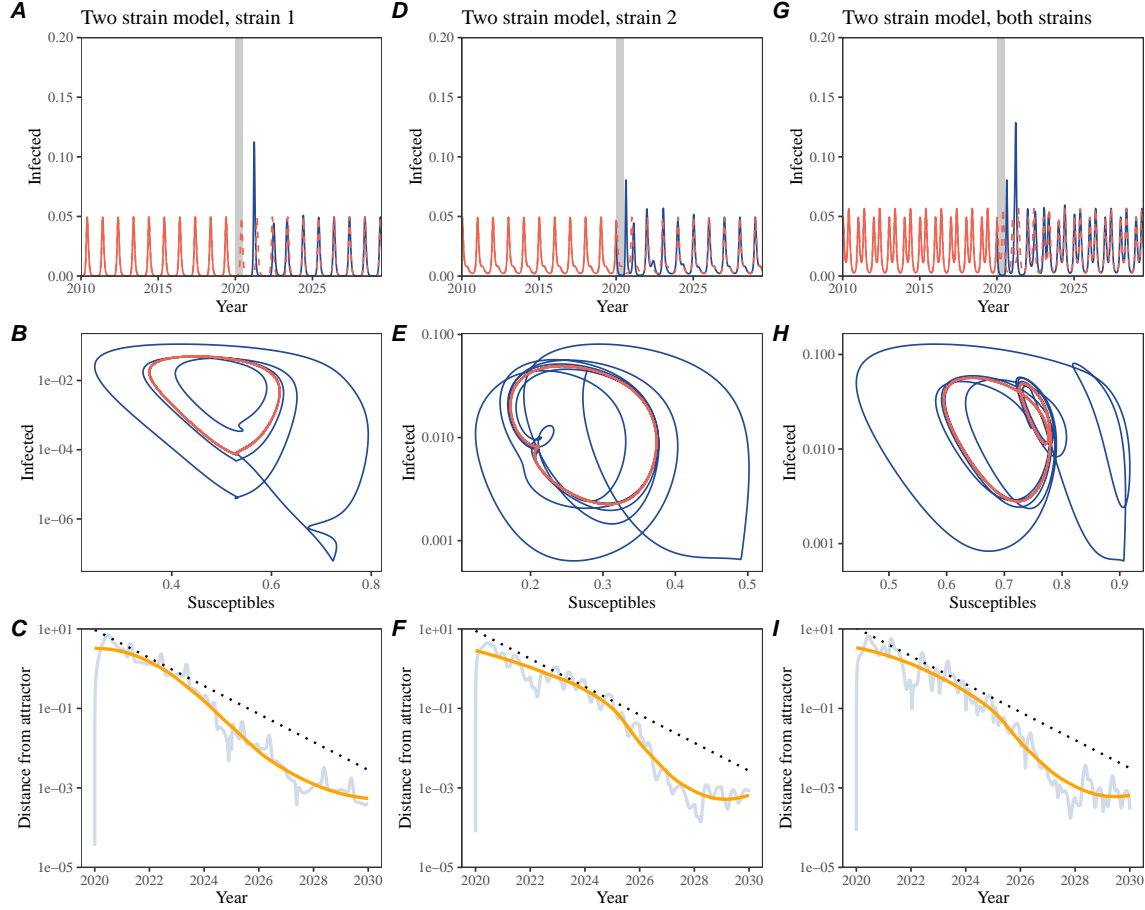


Figure S3: Conceptual framework for measuring pathogen resilience following NPIs for a multi-strain system with seasonal forcing. (A, D, G) Simulated epidemic trajectories using a multi-strain system with seasonal forcing (amplitude of 0.2). Red and blue solid lines represent epidemic dynamics before and after interventions are introduced, respectively. Red dashed lines represent counterfactual epidemic dynamics in the absence of interventions. Gray regions indicate the duration of interventions. (B, E, H) Phase plane representation of the corresponding model. Red and blue solid lines represent epidemic trajectories on an SI phase plane before and after interventions are introduced, respectively. (C, F, I) Changes in logged distance from the attractor over time. Blue lines represent the logged distance from the attractor. Orange lines represent the locally estimated scatterplot smoothing (LOESS) fits to the logged distance from the attractor. Dotted lines are superimposed as a comparison to have the same slope as the intrinsic resilience of the seasonally unforced system.

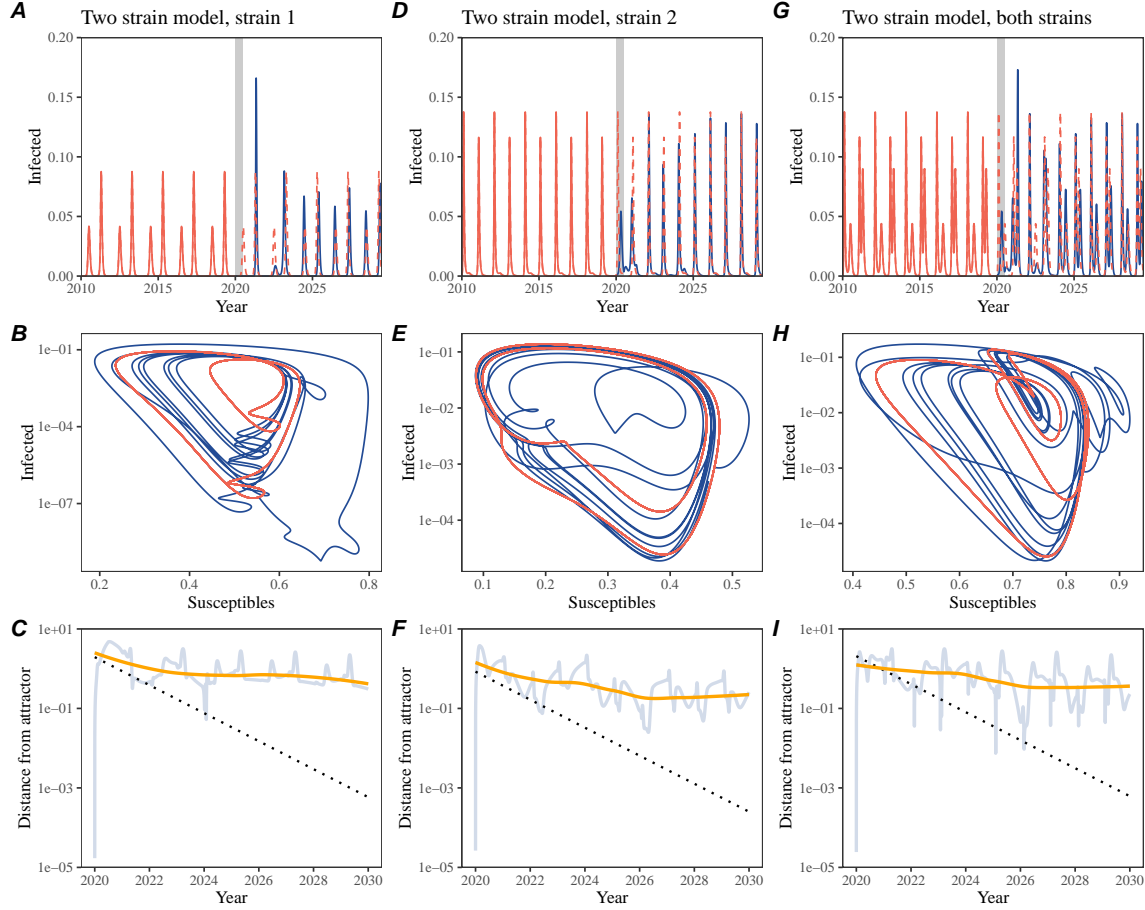


Figure S4: Conceptual framework for measuring pathogen resilience following NPIs for a multi-strain system with strong seasonal forcing. (A, D, G) Simulated epidemic trajectories using a multi-strain system with seasonal forcing (amplitude of 0.4). Red and blue solid lines represent epidemic dynamics before and after interventions are introduced, respectively. Red dashed lines represent counterfactual epidemic dynamics in the absence of interventions. Gray regions indicate the duration of interventions. (B, E, H) Phase plane representation of the corresponding model. Red and blue solid lines represent epidemic trajectories on an SI phase plane before and after interventions are introduced, respectively. (C, F, I) Changes in logged distance from the attractor over time. Blue lines represent the logged distance from the attractor. Orange lines represent the locally estimated scatterplot smoothing (LOESS) fits to the logged distance from the attractor. Dotted lines are superimposed as a comparison to have the same slope as the intrinsic resilience of the seasonally unforced system.

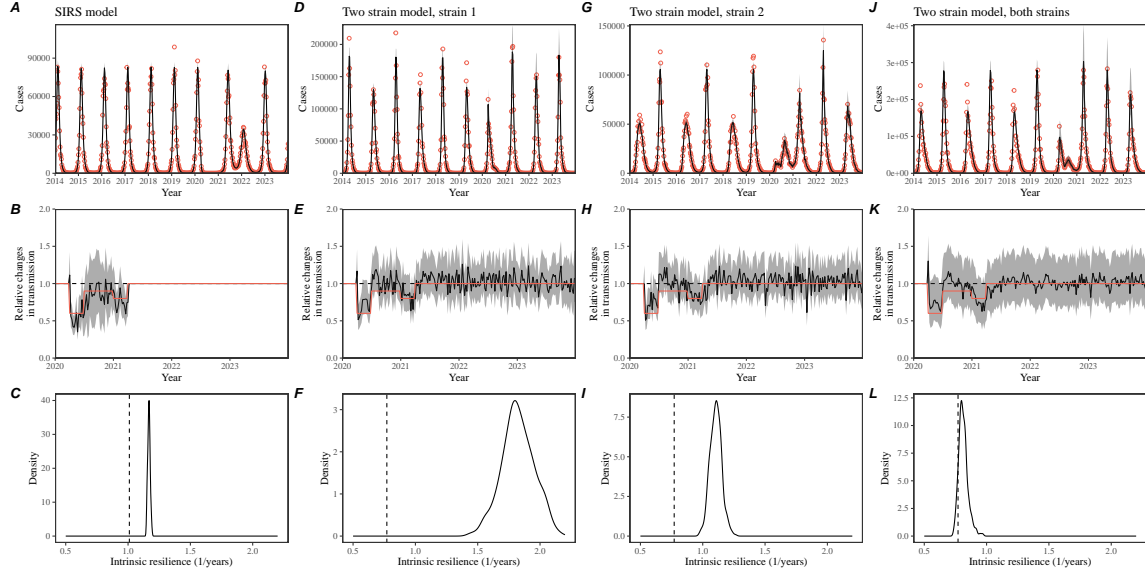


Figure S5: Mechanistic model fits to simulated data and inferred intrinsic resilience. (A, D, G, J) Simulated case time series from corresponding models (red) and SIRS model fits (black). (B, E, H, K) Assumed changes in transmission due to pandemic NPIs (red) and estimated changes from the SIRS model (black). Solid lines and shaded regions represent fitted posterior median and 95% credible intervals. (C, F, I, L) True intrinsic resilience of the seasonally unforced system (vertical lines) and the posterior distribution of the inferred intrinsic resilience from the SIRS model (density plots).

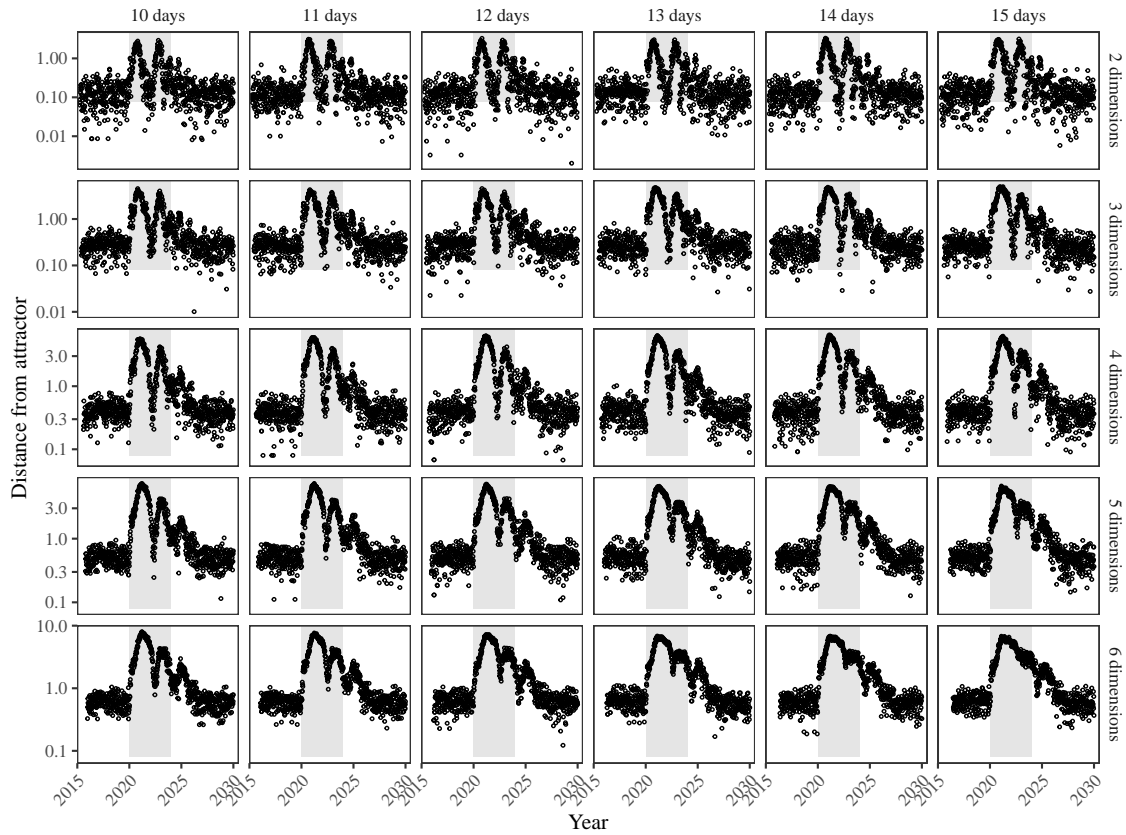


Figure S6: Sensitivity of the distance from the attractor to choices about embedding lags and dimensions. Sensitivity analysis for the distance-from-attractor time series shown in Figure 3E in the main text by varying the embedding lag between 10–15 days and embedding dimensions between 2–6 dimensions.

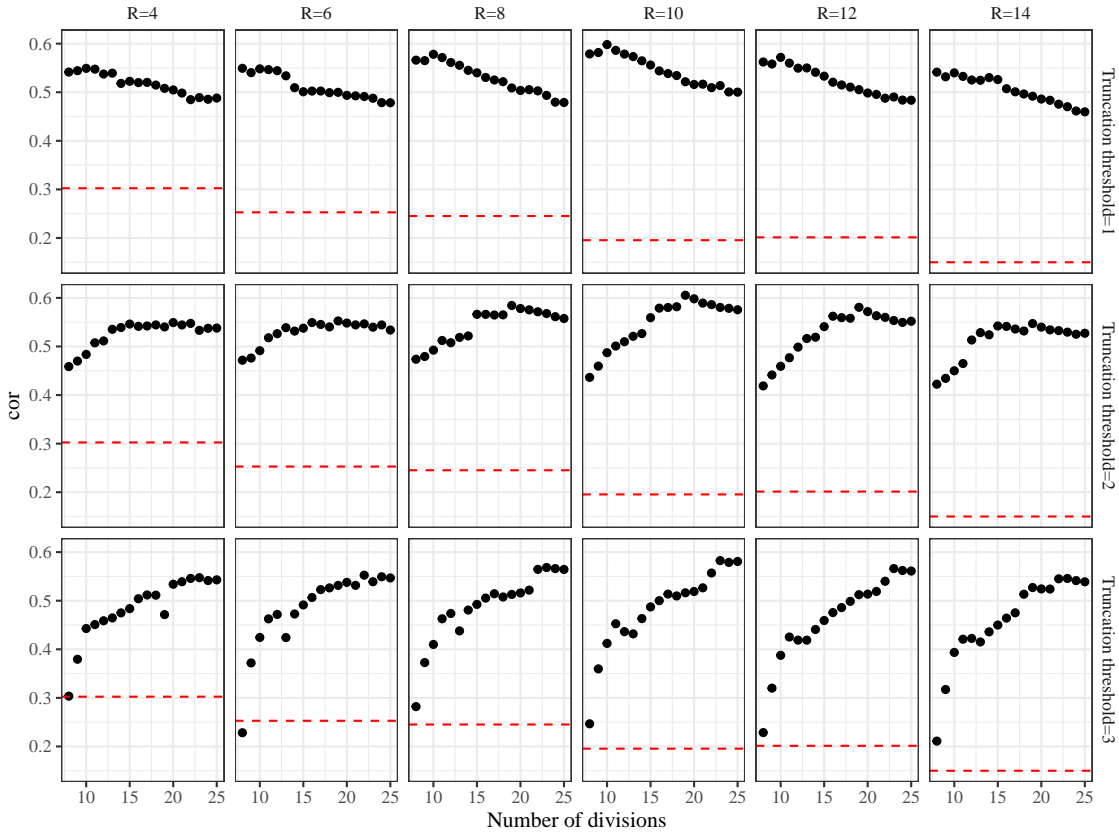


Figure S7: Impact of fitting window selection on the estimation of empirical resilience. We simulated 500 epidemics of a stochastic SIRS model with randomly drawn parameters and randomly generated intervention impacts. For each simulation, we reconstructed the empirical attractor based on the approach outlined in Figure 3 and estimate the distance from the attractor. The naive approach fits a linear regression on a log scale, starting from the maximum distance until the end of the time series. The window-based approach tries to select an appropriate window by smoothing the distance estimates and finding the time period when the smoothed time series crosses pre-determined threshold, relative to the maximum distance; then, a linear regression is fitted by using the raw distance within this time period.

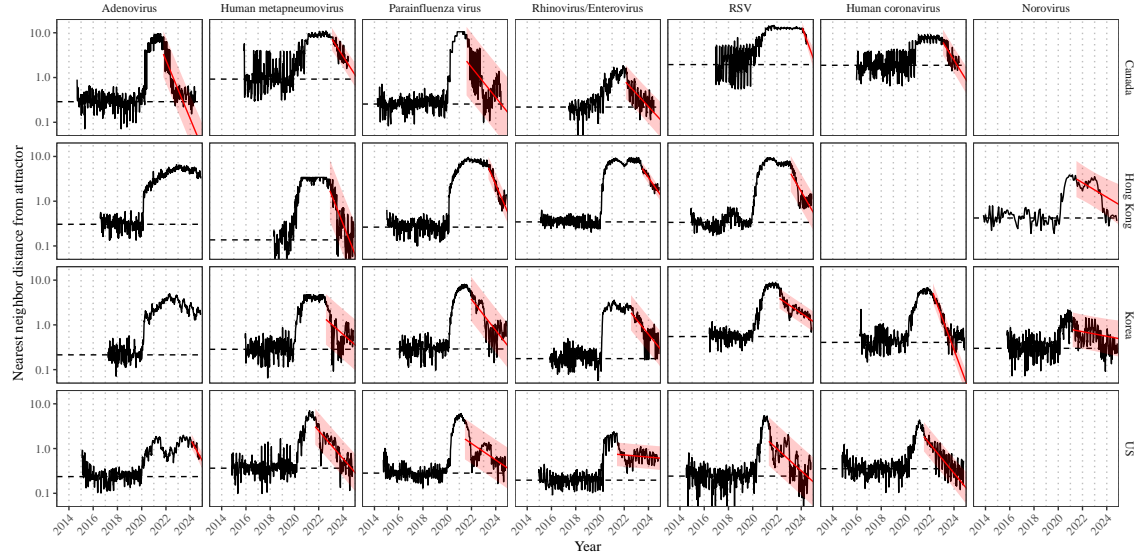


Figure S8: Estimated time series of distance from the attractor for each pathogen and corresponding linear regression fits using automated window selection criterion across Canada, Hong Kong, Korea, and the US. Black lines represent the estimated distance from the attractor. Red lines and shaded regions represent the linear regression fits and corresponding 95% confidence intervals. Dashed lines represent the average of the pre-pandemic nearest neighbor distances.

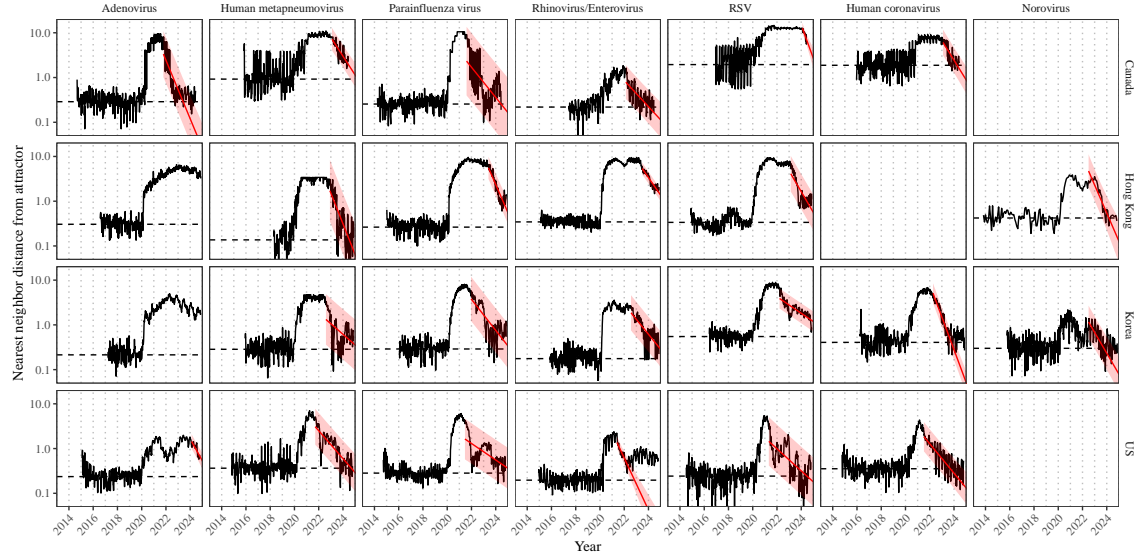


Figure S9: Estimated time series of distance from the attractor for each pathogen and corresponding linear regression fits across Canada, Hong Kong, Korea, and the US, including ad-hoc regression window selection. We used ad-hoc regression windows for norovirus in Hong Kong and Korea and Rhinovirus/Enterovirus in the US. Black lines represent the estimated distance from the attractor. Red lines and shaded regions represent the linear regression fits and corresponding 95% confidence intervals. Dashed lines represent the average of the pre-pandemic nearest neighbor distances.

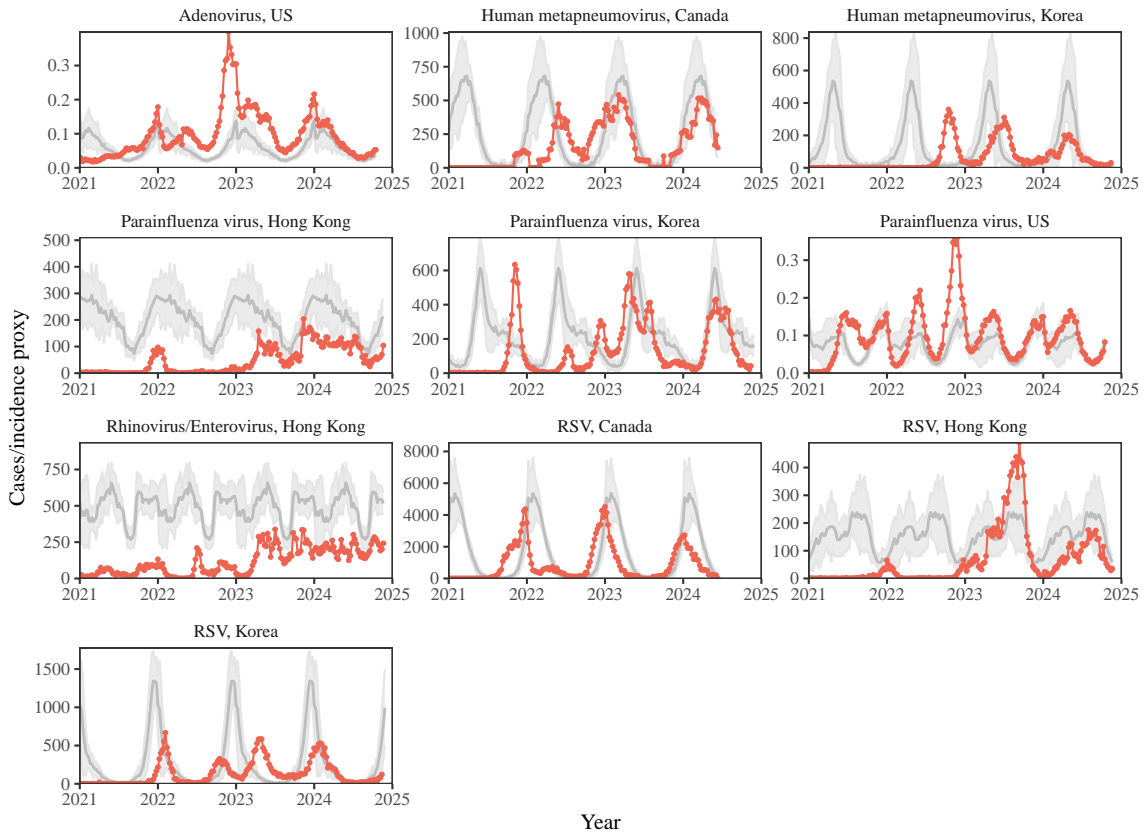


Figure S10: Observed dynamics for pathogen that are predicted to return after the end of 2024. Red points and lines represent data before 2020. Gray lines and shaded regions represent the mean seasonal patterns and corresponding 95% confidence intervals around the mean, previously shown in Figure 1.

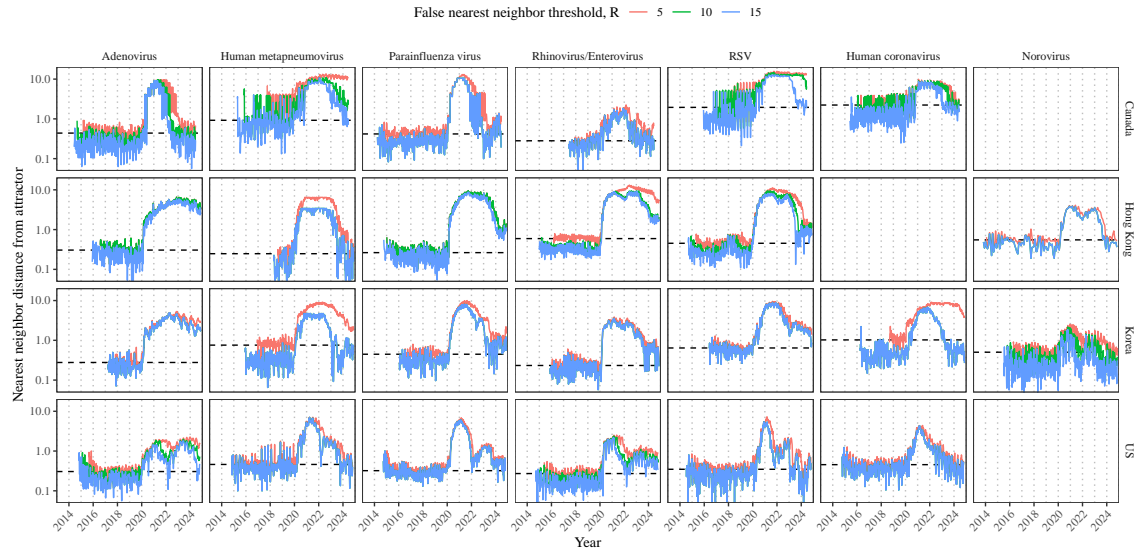


Figure S11: Estimated time series of distance from the attractor for each pathogen across different choices about false nearest neighbor threshold values. Using higher threshold values for the false nearest neighbor approach gives lower embedding dimensions. Colored lines represent the estimated distance from the attractor for different threshold values.

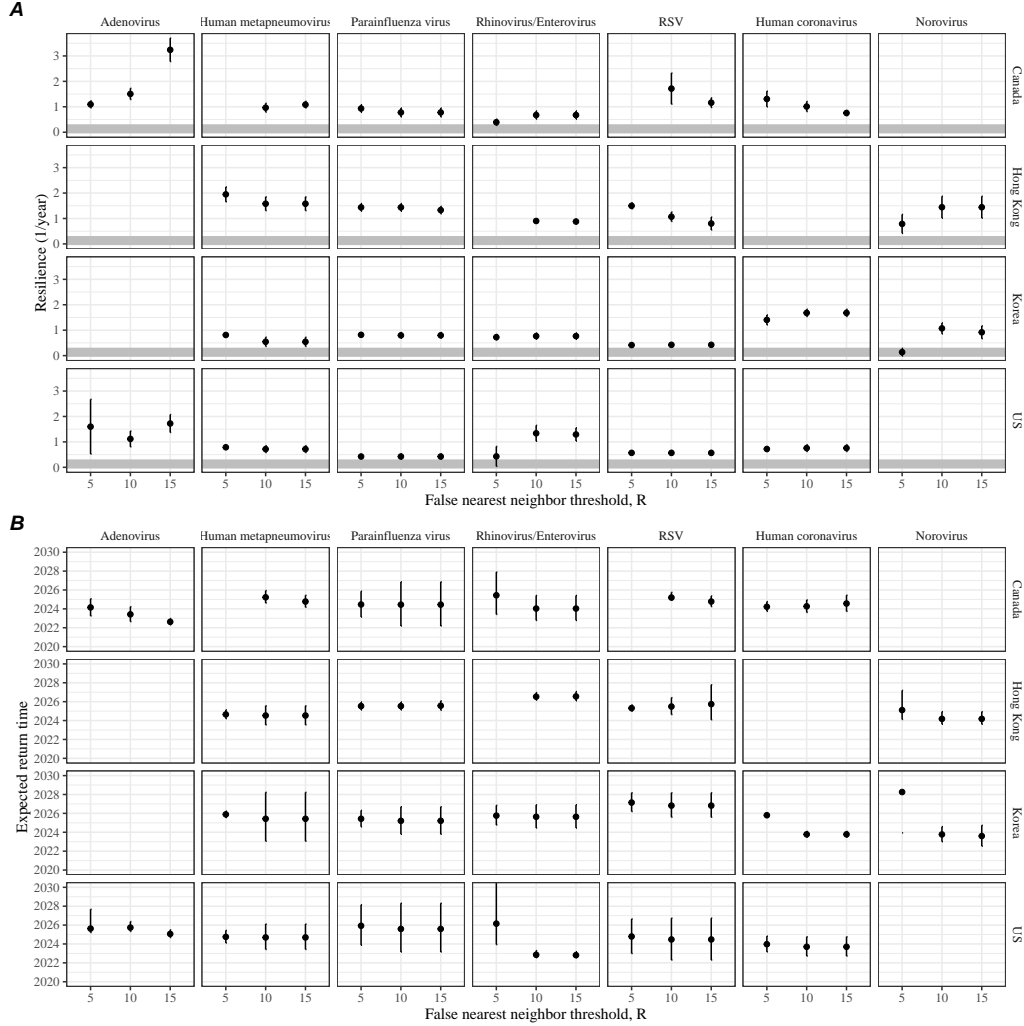


Figure S12: Summary of resilience estimates and predictions for return time across different choices about false nearest neighbor threshold values. The automated window selection method was used for all scenarios to estimate pathogen resilience, except for norovirus in Hong Kong and Korea and Rhinovirus/Enterovirus in the US. We used the same ad-hoc regression windows for norovirus in Hong Kong and Korea and Rhinovirus/Enterovirus in the US as we did in the main analysis. (A) Estimated pathogen resilience. The gray horizontal line represents the intrinsic resilience of pre-vaccination measles dynamics. (B) Predicted timing of when each pathogen will return to their pre-pandemic cycles. The dashed line in panel B indicates the end of 2024 (current observation time). Error bars represent 95% confidence intervals.

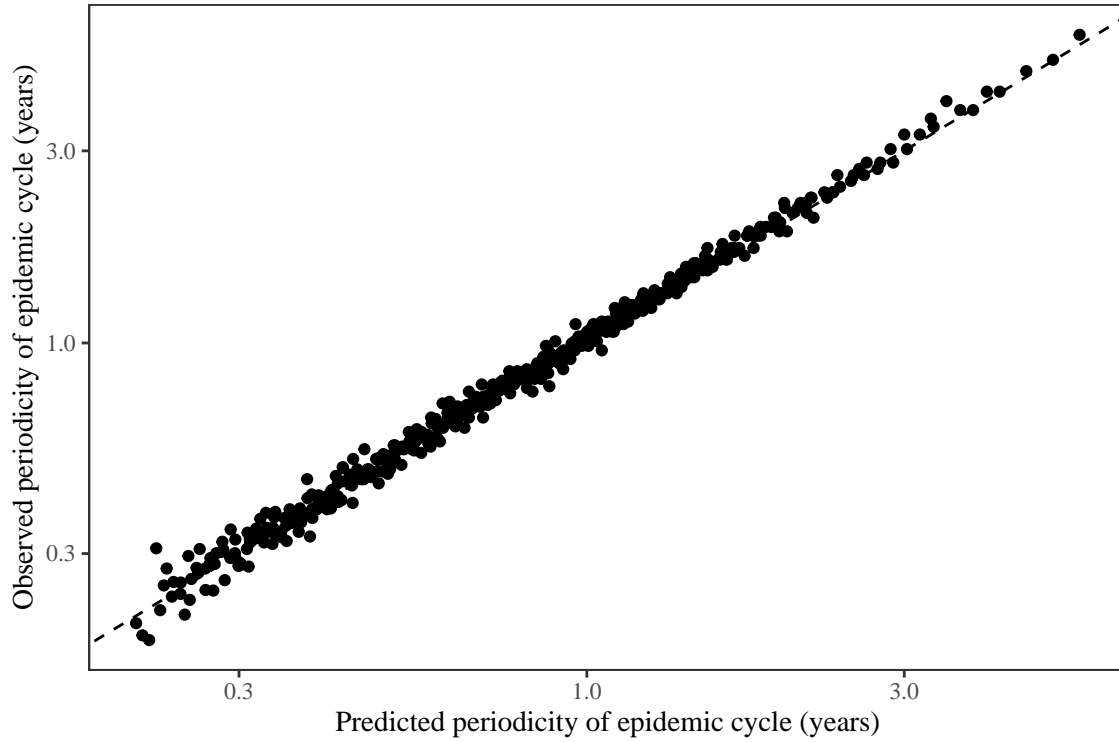


Figure S13: **Comparison between the observed and predicted periodicity of the epidemic cycle of the seasonally unforced SIRS model.** The observed periodicity of the epidemic corresponds to the periodicity at which maximum spectral density occurs. The predicted periodicity of the epidemic corresponds to $2\pi/\text{Im}(\lambda)$, where $\text{Im}(\lambda)$ is the imaginary part of the eigenvalue.

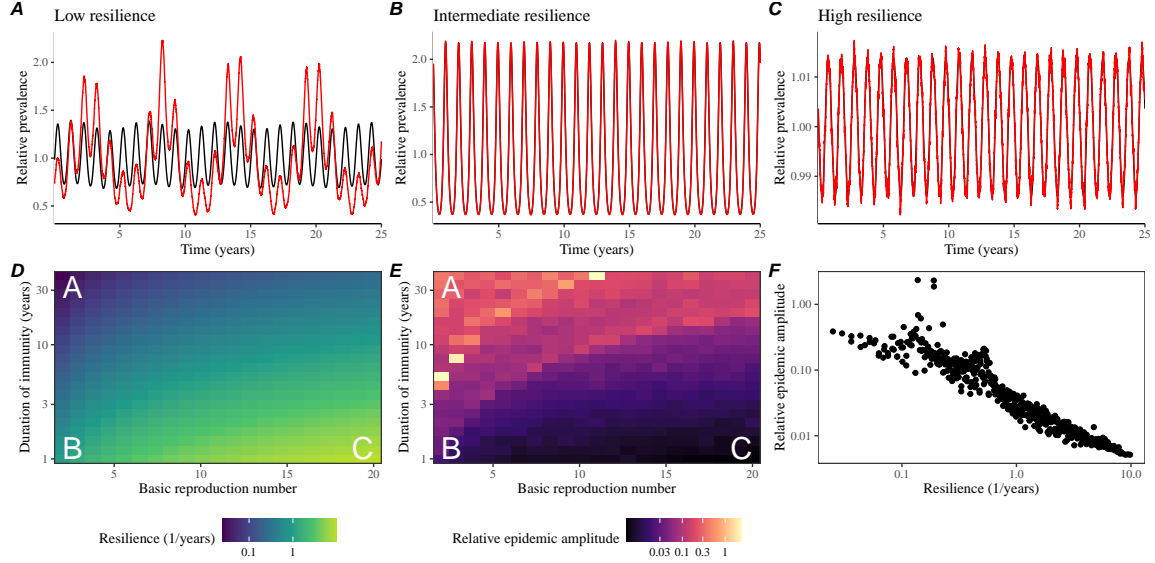


Figure S14: Linking resilience of a host-pathogen system to its sensitivity to stochastic perturbations for the seasonally forced SIRS model. (A–C) Epidemic trajectories of a stochastic SIRS model across three different resilience values: low, intermediate, and high. The relative prevalence was calculated by dividing infection prevalence by its mean value. (D) The heat map represents the intrinsic resilience of the seasonally unforced system as a function of the basic reproduction number \mathcal{R}_0 and the duration of immunity. (E) The heat map represents the relative epidemic amplitude as a function of the basic reproduction number \mathcal{R}_0 and the duration of immunity. To calculate the relative epidemic amplitude, we first take the relative difference in infection prevalence between stochastic and deterministic trajectories: $\epsilon = (I_{\text{stoch}} - I_{\text{det}})/I_{\text{det}}$. Then, we calculate the difference between maximum and minimum of the relative difference and divide by half: $(\max \epsilon - \min \epsilon)/2$. (F) The relationship between pathogen resilience and relative epidemic amplitude.

687 **References**

- 688 [1] Rachel E Baker, Sang Woo Park, Wenchang Yang, Gabriel A Vecchi, C Jessica E
689 Metcalf, and Bryan T Grenfell. The impact of COVID-19 nonpharmaceutical
690 interventions on the future dynamics of endemic infections. *Proceedings of the*
691 *National Academy of Sciences*, 117(48):30547–30553, 2020.
- 692 [2] Gabriela B Gomez, Cedric Mahé, and Sandra S Chaves. Uncertain effects of the
693 pandemic on respiratory viruses. *Science*, 372(6546):1043–1044, 2021.
- 694 [3] Mihaly Koltai, Fabienne Krauer, David Hodgson, Edwin van Leeuwen, Marina
695 Treskova-Schwarzbach, Mark Jit, and Stefan Flasche. Determinants of RSV
696 epidemiology following suppression through pandemic contact restrictions. *Epi-*
697 *demics*, 40:100614, 2022.
- 698 [4] Sang Woo Park, Brooklyn Noble, Emily Howerton, Bjarke F Nielsen, Sarah
699 Lentz, Lilliam Ambroggio, Samuel Dominguez, Kevin Messacar, and Bryan T
700 Grenfell. Predicting the impact of non-pharmaceutical interventions against
701 COVID-19 on *Mycoplasma pneumoniae* in the United States. *Epidemics*,
702 49:100808, 2024.
- 703 [5] Amanda C Perofsky, Chelsea L Hansen, Roy Burstein, Shanda Boyle, Robin
704 Prentice, Cooper Marshall, David Reinhart, Ben Capodanno, Melissa Truong,
705 Kristen Schwabe-Fry, et al. Impacts of human mobility on the citywide trans-
706 mission dynamics of 18 respiratory viruses in pre-and post-COVID-19 pandemic
707 years. *Nature communications*, 15(1):4164, 2024.
- 708 [6] Eric J Chow, Timothy M Uyeki, and Helen Y Chu. The effects of the COVID-19
709 pandemic on community respiratory virus activity. *Nature Reviews Microbiol-*
710 *ogy*, 21(3):195–210, 2023.
- 711 [7] Stephen M Kissler, Christine Tedijanto, Edward Goldstein, Yonatan H Grad,
712 and Marc Lipsitch. Projecting the transmission dynamics of SARS-CoV-2
713 through the postpandemic period. *Science*, 368(6493):860–868, 2020.
- 714 [8] Rachel E Baker, Chadi M Saad-Roy, Sang Woo Park, Jeremy Farrar, C Jessica E
715 Metcalf, and Bryan T Grenfell. Long-term benefits of nonpharmaceutical inter-
716 ventions for endemic infections are shaped by respiratory pathogen dynamics.
717 *Proceedings of the National Academy of Sciences*, 119(49):e2208895119, 2022.
- 718 [9] John-Sebastian Eden, Chisha Sikazwe, Ruopeng Xie, Yi-Mo Deng, Sheena G
719 Sullivan, Alice Michie, Avram Levy, Elena Cutmore, Christopher C Blyth,
720 Philip N Britton, et al. Off-season RSV epidemics in Australia after easing
721 of COVID-19 restrictions. *Nature communications*, 13(1):2884, 2022.
- 722 [10] Stuart L Pimm. The structure of food webs. *Theoretical population biology*,
723 16(2):144–158, 1979.

- 724 [11] Michael G Neubert and Hal Caswell. Alternatives to resilience for measuring
725 the responses of ecological systems to perturbations. *Ecology*, 78(3):653–665,
726 1997.
- 727 [12] Lance H Gunderson. Ecological resilience—in theory and application. *Annual
728 review of ecology and systematics*, 31(1):425–439, 2000.
- 729 [13] Vasilis Dakos and Sonia Kéfi. Ecological resilience: what to measure and how.
730 *Environmental Research Letters*, 17(4):043003, 2022.
- 731 [14] Floris Takens. Detecting strange attractors in turbulence. In *Dynamical Sys-
732 tems and Turbulence, Warwick 1980: proceedings of a symposium held at the
733 University of Warwick 1979/80*, pages 366–381. Springer, 2006.
- 734 [15] Jonathan Dushoff, Joshua B Plotkin, Simon A Levin, and David JD Earn. Dynamical resonance can account for seasonality of influenza epidemics. *Pro-
735 ceedings of the National Academy of Sciences*, 101(48):16915–16916, 2004.
- 736 [16] Alan Hastings, Karen C Abbott, Kim Cuddington, Tessa Francis, Gabriel Gell-
737 ner, Ying-Cheng Lai, Andrew Morozov, Sergei Petrovskii, Katherine Scran-
738 ton, and Mary Lou Zeeman. Transient phenomena in ecology. *Science*,
739 361(6406):eaat6412, 2018.
- 740 [17] Matthew B Kennel, Reggie Brown, and Henry DI Abarbanel. Determining
741 embedding dimension for phase-space reconstruction using a geometrical con-
742 struction. *Physical review A*, 45(6):3403, 1992.
- 743 [18] Eugene Tan, Shannon Algar, Débora Corrêa, Michael Small, Thomas Stemler,
744 and David Walker. Selecting embedding delays: An overview of embedding
745 techniques and a new method using persistent homology. *Chaos: An Interdis-
746 ciplinary Journal of Nonlinear Science*, 33(3), 2023.
- 747 [19] Samit Bhattacharyya, Per H Gesteland, Kent Korgenski, Ottar N Bjørnstad,
748 and Frederick R Adler. Cross-immunity between strains explains the dynamical
749 pattern of paramyxoviruses. *Proceedings of the National Academy of Sciences*,
750 112(43):13396–13400, 2015.
- 751 [20] Bryan T Grenfell, Ottar N Bjørnstad, and Bärbel F Finkenstädt. Dynamics of
752 measles epidemics: scaling noise, determinism, and predictability with the TSIR
753 model. *Ecological monographs*, 72(2):185–202, 2002.
- 754 [21] Virginia E Pitzer, Cécile Viboud, Vladimir J Alonso, Tanya Wilcox, C Jessica
755 Metcalf, Claudia A Steiner, Amber K Haynes, and Bryan T Grenfell. Environ-
756 mental drivers of the spatiotemporal dynamics of respiratory syncytial virus in
757 the United States. *PLoS pathogens*, 11(1):e1004591, 2015.

- 759 [22] Katharine R Dean, Fabienne Krauer, Lars Walløe, Ole Christian Lingjærde, Bar-
760 bara Bramanti, Nils Chr Stenseth, and Boris V Schmid. Human ectoparasites
761 and the spread of plague in Europe during the Second Pandemic. *Proceedings*
762 *of the National Academy of Sciences*, 115(6):1304–1309, 2018.
- 763 [23] Margarita Pons-Salort and Nicholas C Grassly. Serotype-specific immunity
764 explains the incidence of diseases caused by human enteroviruses. *Science*,
765 361(6404):800–803, 2018.
- 766 [24] Sarah Cobey and Edward B Baskerville. Limits to causal inference with state-
767 space reconstruction for infectious disease. *PLoS one*, 11(12):e0169050, 2016.
- 768 [25] Edward Goldstein, Sarah Cobey, Saki Takahashi, Joel C Miller, and Marc Lip-
769 sitch. Predicting the epidemic sizes of influenza A/H1N1, A/H3N2, and B: a
770 statistical method. *PLoS medicine*, 8(7):e1001051, 2011.
- 771 [26] Bob Carpenter, Andrew Gelman, Matthew D Hoffman, Daniel Lee, Ben
772 Goodrich, Michael Betancourt, Marcus A Brubaker, Jiqiang Guo, Peter Li,
773 and Allen Riddell. Stan: A probabilistic programming language. *Journal of*
774 *statistical software*, 76, 2017.
- 775 [27] Stan Development Team. RStan: the R interface to Stan, 2024. R package
776 version 2.32.6.